

RICE UNIVERSITY

**Optically Detected Terahertz Resonance
Spectroscopy of Semiconductor Nanostructures**

by

Rahul Srivastava

A THESIS SUBMITTED
IN PARTIAL FULFILLMENT OF THE
REQUIREMENTS FOR THE DEGREE

Master of Science

APPROVED, THESIS COMMITTEE:

Junichiro Kono, Chair
Assistant Professor of Electrical and
Computer Engineering

Frank K. Tittel
J. S. Abercrombie Professor of Electrical
and Computer Engineering

Daniel M. Mittleman
Associate Professor of Electrical and
Computer Engineering

Houston, Texas

April, 2005

ABSTRACT

Optically Detected Terahertz Resonance Spectroscopy of Semiconductor Nanostructures

by

Rahul Srivastava

In this dissertation work we have developed an ultracompact optically-detected terahertz resonance (ODTR) spectroscopy system, using quantum cascade lasers (QCLs). This system can be used for investigating various terahertz (THz) resonances in semiconductors. We use a THz QCL, of an appropriate frequency, operating in the close vicinity of the sample. Due to the small size of the QCLs, we can mount them on the sample holder of the magnet, which allows focusing of the THz beam onto the sample with minimal loss. This precludes the need of any external source of radiation. We use a single fiber to send the pump laser beam to the sample and collect the PL signal. The use of the fiber makes our system versatile enough to be used in a variety of situations, especially inside our magnet. We have used this setup to obtain some preliminary ODTR data on an InGaAs/AlGaAs multiple-quantum well sample.

Acknowledgments

I would like to thank many people who have made this thesis work a learning and enjoyable experience. First and foremost, I would like to express my gratitude towards my thesis advisor, Dr. Junichiro Kono, for all his advice, support, guidance and encouragement during my research. He has been a constant source of motivation and extremely approachable throughout this work. Next, I would like to thank Dr. Daniel Mittleman and Prof. Frank Tittel for agreeing to participate on my thesis committee.

I would like to thank Dr. Giti Khodaparast for providing expert guidance during the initial phases of this project and also teaching me various laboratory skills. I am thankful to Ajit Srivastava and Jigang Wang for their constant encouragement by helping me in my experiments and valuable discussions about Physics. I would like to thank Diane Larrabee and Sasa Zaric for patiently teaching me different laboratory techniques. I am thankful to Xiangfeng Wang for helping me in my experiments. Thanks are also due to my colleagues, Dr. Gordana Ostojic, Yusuke Hashimoto, Chanjuan Sun and Cliff Wong for their support and providing a thoughtful, pleasant and conducive atmosphere for research.

I would like to thank Prof. Jérôme Faist and his group at the University of Neuchâtel for providing the excellent terahertz quantum cascade lasers. Special thanks are due to Giacomo Scalari for his helpful suggestions, information and ideas on the use of quantum cascade lasers.

I would like to express my gratitude towards Dr. Alexander Rimberg, whose superconducting magnet and lab space we used for the course of this project. I am

also grateful to his graduate students, Joy Sarkar, Madhu Thalakulam, Tim Gilheart and Zhongqing Ji for helping me with the use of their magnet and other lab equipment.

I would like to thank Michael Dye for providing me with lab equipment for the experiment. I would like to thank Dwight Dear and his colleagues at the Research Support Shop for helping with the design and fabrication of the various customised components required for the experimental setup.

I would like to thank my friends at Rice, especially Supratik Majumder, Dharm-pal Takhar, Sampad Laha, Ravi Ranjan Kumar, Kartik Mutnuri, Arnab Nandi and Chris Martinez for giving encouragement and support through the various stages of this project. I would like to thank Sindhu Tatimatla for being supportive and understanding under difficult circumstances. Finally, I would like to thank my parents and sister for their love, support and sacrifices.

Contents

Abstract	ii
Acknowledgments	iii
List of Illustrations	viii
1 Introduction	1
1.1 Outline	3
2 Optically Detected Terahertz Resonance (ODTR) in Semi-conductors	4
2.1 Introduction	4
2.2 Background	5
2.2.1 Microwave-ODR	5
2.2.2 FIR-ODR	6
2.3 Advantages Over Conventional Resonance Methods	7
2.4 Different Types of Optically Detected Resonances	9
3 Terahertz Quantum Cascade Lasers	17
3.1 The Terahertz Gap	17
3.2 Quantum Cascade Lasers	18
3.2.1 Operation	19
3.3 Terahertz Quantum Cascade Lasers	22
3.3.1 Chirped Superlattice Structures Based QCLs	23

3.3.2	Resonant Phonon Scattering Based QCLs	25
3.3.3	Bound-to-Continuum Transition Based QCLs	25
3.4	THz QCLs in Magnetic Field	26
4	Experimental Methods	32
4.1	ODTR Setup	32
4.2	Lasers	34
4.2.1	Argon-Ion Laser	34
4.2.2	Quantum Cascade Laser	36
4.3	Superconducting Magnet	37
4.4	Sample Stick and Holder	39
4.5	Dichroic Mirror and Filters	42
4.6	Optical Fiber and Associated Optics	43
4.7	Lock-in Detection Techniques	43
4.8	Samples Used	44
4.8.1	InGaAs/AlGaAs Multiple Quantum Well	44
4.8.2	Quantum Dots	44
4.8.3	Dilute Magnetic Semiconductors	44
5	Results and Discussion	47
5.1	Magnetic Field Dependent PL	47
5.2	Temperature Dependent PL	50
5.3	Shubnikov-de Haas (Magneto-Transport) Effect	52
5.4	Optically Detected Resonance	53
6	Summary and Future Work	55
6.1	ODTR Study of Other Nanostructures	55

6.2 Spin Resonance Studies	55
6.3 ODTR Study of Excitons in Carbon Nanotubes	56
Bibliography	59

Illustrations

1.1	An illustration of the terahertz technology gap	2
2.1	An illustration of ODR type experiments. An external field induces splitting of the energy levels which leads to a change in photoluminescence signal at resonance conditions	9
2.2	Experimental setup for OD-ESR type experiments [23]	10
2.3	Optically detected ESR lines for GaAs, $\text{Ga}_{1-x}\text{In}_x\text{As}$ and $\text{Ga}_{1-x}\text{Al}_x\text{As}$ at 1.7K (field in gauss, rf frequency 151 MHz) [23]	11
2.4	Experimental setup for FIR-ODCR type experiments [20]	12
2.5	Optically detected CR and exciton resonance (ER) lines. The ratio of the PL amplitude with and without FIR irradiation for GaAs/AlGaAs quantum wells [21]	14
2.6	Comparison of the experimental results to the calculations of the energy of various FIR resonances in GaAs/AlGaAs quantum wells as a function of magnetic field [21]	16
3.1	Present QCL operation ranges (http://www.unine.ch/phys/meso/)	18
3.2	Schematic conduction band energy diagram of two QCL active regions with intermediate injector region [26]	20

3.3	(a) Chirped superlattice design (b) calculated population inversion and current density [1]	24
3.4	(a) Bound-to-continuum type QCL conduction band profile [30]	26
3.5	Chirped superlattice type QCL emission intensity as a function of the magnetic field [33]	28
4.1	Setup for the ODTR experiment	33
4.2	Photo of the setup for the ODTR experiment	34
4.3	Laser emission lines for the Argon-ion laser (http://www.melles-griot.com)	35
4.4	Schematic diagram of the sample processing for a THz QCL [35]	36
4.5	Photograph of a QCL	37
4.6	Optical power characteristics of the QCL in pulsed mode (Jérôme Faist's group at University of Neuchatel)	38
4.7	Optical power characteristics of the QCL in CW mode (Jérôme Faist's group at University of Neuchatel)	38
4.8	Superconducting magnet used in our experiment (http://www.janis.com)	39
4.9	Design of the sample stick for the ODTR experiment	40
4.10	Design of the sample holder for the ODTR experiment	41
4.11	Photo of the sample holder with the QCL for the ODTR experiment	42
4.12	Energy band calculations of sample 209B	45
4.13	Structure of DMS sample T580	46
5.1	Magnetic field dependent PL data for InGaAs/AlGaAs MQW sample.	48
5.2	Magnetic field dependent PL data for the quantum dot sample	49

5.3	Magnetic field dependant PL data for the dilute magnetic semiconductor (DMS) sample	50
5.4	Temperature dependant PL data for InGaAs/AlGaAs MQW sample .	51
5.5	Shubnikov-de Haas effect in InGaAs/AlGaAs MQW sample	52
5.6	Preliminary ODR data for InGaAs/AlGaAs MQW sample	53
6.1	A schematic diagram showing how the interband excitation energies are higher than the calculated bandgaps	57

Chapter 1

Introduction

The terahertz (THz) region of the electromagnetic spectrum (0.1 - 10 THz; 3000 - 30 μm ; 0.4 - 45 meV) is rich in a number of physical phenomena. A number of low-energy collective and elementary excitations such as phonons, plasmons, magnons, polaritons, polarons, superconducting gap excitation, cyclotron resonance, spin resonance and intersubband transitions are expected and observed in this range. In addition, carrier scattering, recombination and tunneling phenomena in semiconductors are observed in the picosecond time frame, which corresponds to the terahertz region in the frequency domain. The transition between transport and optical phenomena in the frequency domain occurs in this region and, as a result, there is a fascinating interplay of AC electric fields and photons on the physical properties. Despite holding much interest, this spectral range is currently under-utilized due to a wide technology gap that exists between electronics and photonics. The same reasons that make this region interesting have resulted in the lack of convenient sources, detectors and modulators. A variety of coherent and incoherent THz sources exist. CO_2 pumped molecular gas lasers, free electron lasers, synchrotron radiation and hot bodies have been traditionally used for spectroscopy. However, these sources are extremely bulky, requiring a significant infrastructure, or simply too weak for certain applications. Detectors in this region are not fast and sensitive compared to well-advanced detectors in the visible range. Moreover, the recent invention of THz quantum cascade lasers (QCLs) [1] may open up new possibilities in THz spectroscopy. The recent develop-

1.1 Outline

In the next chapter, we review the genesis of optically detected resonance spectroscopy of semiconductors. We will talk about the advantages of this techniques as well as describe some of the phenomena that can be studied with this tool. Chapter 3 deals with the THz QCLs, which are the source for the far-infrared (FIR) radiation in our experiment. We will also review the effects of magnetic field on a THz QCL, as we will be using the laser in a magnetic field. In Chapter 4, we discuss our experimental setup in detail, covering the main components required for our experiment. Our experimental results are presented in the next chapter. Finally, in Chapter 7 we sum up our work and discuss the scope for future study.

Chapter 2

Optically Detected Terahertz Resonance (ODTR) in Semiconductors

2.1 Introduction

Optically detected resonance (ODR) is a general term for detection of various low-energy (MHz to THz) resonances, such as magnetic resonance, cyclotron resonance, etc., optically, i.e., using techniques available in the near-infrared, visible and ultra-violet ranges.

In a conventional microwave/THz resonance experiment, the sample is placed in a microwave cavity/irradiated by a THz source and the external field (e.g., magnetic field) is applied to the sample such that the alternating field of the cavity B_{rf} is normal to B_{ext} . The degeneracy of the electron spin states characterized by the quantum number $m_s = \pm\frac{1}{2}$, is lifted by the application of a magnetic field B_{ext} and transitions between the spin levels are induced by radiation B_{rf} . The ground state is in thermal equilibrium, so when the microwave energy equals the separation between the Zeeman electronic levels of the magnetic ions or defects, resonant absorption of microwave power occurs and is measured. In a typical setup, energy of the field causing transition is held fixed whereas the magnetic field is swept to cause the resonance condition mentioned above.

In optically detected resonance experiments, the sample is also kept in a microwave cavity/irradiated by a THz source, but at the same time photoluminescence (PL) is excited by a laser. Microwave or far-infrared (FIR) resonance is detected through

the changes in PL intensity or polarization while the external field is swept, rather than measuring microwave or FIR absorption directly. ODR techniques offer the advantages of superior resolution and sensitivity over conventional microwave/FIR resonance methods. The application of ODR to the investigations of luminescence processes in solids is well established. These techniques were originally developed from optical pumping studies in gases but are now used in a variety of systems including semiconductor heterostructures.

2.2 Background

2.2.1 Microwave-ODR

Optical detection (OD) techniques of resonance, together with optical pumping, have been used in gases to measure Landé factors, hyperfine constants, and relaxation constants since the 1950s [3]. Initially, in solids, these methods were applied to the study of localized paramagnetic impurities. The first experiments on semiconductors were done in the late 1960s. Optical pumping on delocalized states in semiconductors [4] and optical detection of the conduction-electron polarization [5] were the first experiments.

The first application of OD to electron spin resonance (ODESR) in semiconductors was made by Hermann and Lampel in 1971 [6]. They applied a resonant excitation to the photocreated electronic spins and obtained the conduction electron g -factor value for p -type GaSb. Spin resonance was detected by a change in the polarization of the recombination light.

The first observation of OD of cyclotron resonance (ODCR) was made in Germanium by Baranov using microwaves in 1977 [7]. Cyclotron resonance (CR) was detected, instead of measuring microwave absorption directly, from the change of

the intensity of the electron-hole droplet recombination luminescence while magnetic field was swept. The resonance was registered simultaneously also by determining the change of the absorption of the microwave power in the sample. Romestain and Weisbuch developed this technique for GaAs and CdTe [8]. They were able to establish that the absorption of the microwave power occurring at cyclotron resonance of either type of carrier increases the energy of both the electron and hole gases. The resultant carrier heating can be observed directly by measuring the effective temperature via the shape of optical emission lines or indirectly by monitoring luminescence line intensities. This was an important development as it provided new insights in microwave-carrier-heating studies due to the direct determination of the carrier distribution function. Over the next two decades, this unique technique has been used in the studies of band structures of a variety of semiconductors: e.g., AgBr [9], GaP [10], ZnTe [10], GaAs/Ga_{0.67}Al_{0.33}As multiple quantum well [11], Si [12, 13], Ge [14, 13], ZnSe [13], etc.

It was also pointed out by Romestain and Weisbuch that the large number of optically generated carriers neutralize charged impurities, resulting in an increase of the scattering time τ . This allowed the cyclotron resonance condition $\omega_c\tau \geq 1$ to be fulfilled at low magnetic fields, offering an advantage over conventional absorption CR at low frequencies.

2.2.2 FIR-ODR

The next major development in this field was brought about with the extension of the energy range from microwave to the far-infrared (FIR). The extension of the resonant frequencies to the FIR range was expected to provide further improvements in the value of $\omega\tau$, resulting in a significant enhancement in the resolution and sensitivity of the technique.

The first experiment in this energy range, i.e., FIR-ODCR was reported by Wright *et al.* [15]. The FIR radiation was generated by a CO₂ pumped molecular gas laser. The authors reported, in one experiment, observation of electron and light-hole cyclotron resonance in GaAs, as well as the donor $1s \rightarrow 2p_+$ transitions. Valence band quantum effects were resolved in GaAs and the electron cyclotron resonances displayed a strong spin doublet in the highest quality samples examined. The remarkable resolution and sensitivity of this technique made it possible to observe $n = 1$ to 2 (polaron shifted) and higher spin doublet split resonances at helium temperature with low FIR laser power. Subsequently, FIR-ODCR studies of InP and GaAs [16], GaAs MQWs [17], and GaAs_{1-x}P_x [18] have been reported. In 1994-95, the technique of FIR-ODR was used to observe impurity transitions [19, 20], and internal transitions of excitons [21, 22].

In FIR-ODR experiments, typically, a monochromatic FIR laser beam excites electronic transitions whose energies are tuned into resonance with an applied external field (e.g. magnetic field). Under resonant conditions, the FIR absorption induces changes in the intensity of the band-edge luminescence that is excited by a separate laser whose photon energy is larger than the effective bandgap of the semiconductor nanostructure under investigation.

2.3 Advantages Over Conventional Resonance Methods

The use of conventional microwave resonance methods have been limited to the study of a few semiconductors, viz., Si, Ge and InSb, either for holes or electrons, seldom for both. The constraints are due to the fact that microwave detection requires large monocrystals having a low conductivity to maintain good cavity qualities. Such low conductivity is achieved only by exceptionally high-quality crystals with a very low carrier density, which automatically precludes detection of, e.g., cyclotron resonance.

The advantages of ODTR over conventional THz resonance methods are manifold. For ODTR spectroscopy, doping is not necessary. This permits the study of materials for which doping is difficult, e.g., wide-bandgap semiconductors. The remarkable resolution and sensitivity in measurements afforded by this technique offers a powerful tool to investigate weak as well as narrow lines. In addition, it makes it possible to study the line shapes. The condition $\omega_c\tau \geq 1$ is satisfied at lower fields for ODCR experiments because of the light-induced impurity neutralization. As a result, the low-field limit where conventional resonance methods do not fulfil the $\omega_c\tau$ requirement can be studied.

The optical detection methods permit the investigation of spotlight-size samples, single crystallites of polycrystalline material or inhomogeneous samples like epilayer alloys. Impurity distribution can be tested via mobility variations to a scale unattainable by standard transport measurements.

Another major advantage is in the possibility of selecting spectrally a specific photoluminescence (PL) feature, among the various band-edge features, as the detection “channel.” Since the PL spectra from semiconductors involve free excitons, bound excitons, and band-to-impurity, impurity-to-band, or impurity-impurity (donor-acceptor) recombination lines, it is possible to use the specificity of the FIR spectrum to obtain information about recombination mechanisms and the interactions that give rise to the various lines. For new materials or structures, the combination of FIR resonance and PL could permit the identification of particular features in the PL spectrum.

The “detection” of the resonance signal is done in the visible or the near infrared (NIR) range. The technology that is available for the visible and NIR regions of the spectrum as regards to detectors and modulators is well-developed as compared to the FIR. The combination of these factors make this technique so unique and exciting

for semiconductor spectroscopy.

2.4 Different Types of Optically Detected Resonances

The general resonance condition is given by the following equation.

$$\Delta E_{split} = \hbar\omega \quad (2.1)$$

Where $\hbar\omega$ is the energy of the microwave or THz radiation. It is this absorption of energy, which is detected as a change in PL in an optically detected resonance experiment. This gives important information about various physical parameters such as the g -factor, effective mass of charge carriers, electron mobility spin-relaxation time

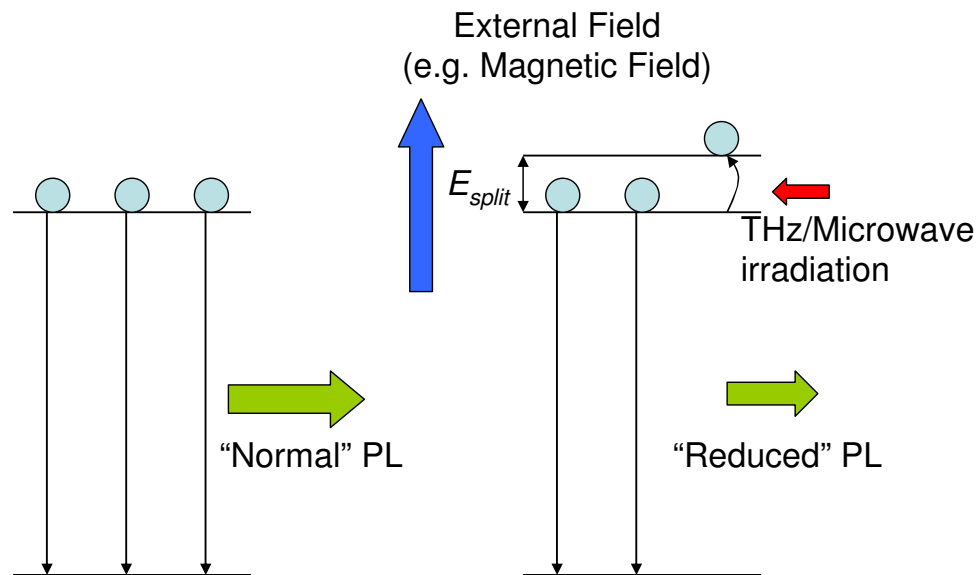


Figure 2.1 : An illustration of ODR type experiments. An external field induces splitting of the energy levels which leads to a change in photoluminescence signal at resonance conditions

Optically detected magnetic resonance involves application of an external magnetic field to cause Zeeman splitting of degenerate spin states. These spin states could be that of a nuclei (as in NMR) or electrons (as in ESR) in different environments. These split-levels can then absorb radiation of appropriate frequency (radio frequency for NMR, microwave for ESR, etc) when it is resonant with them.

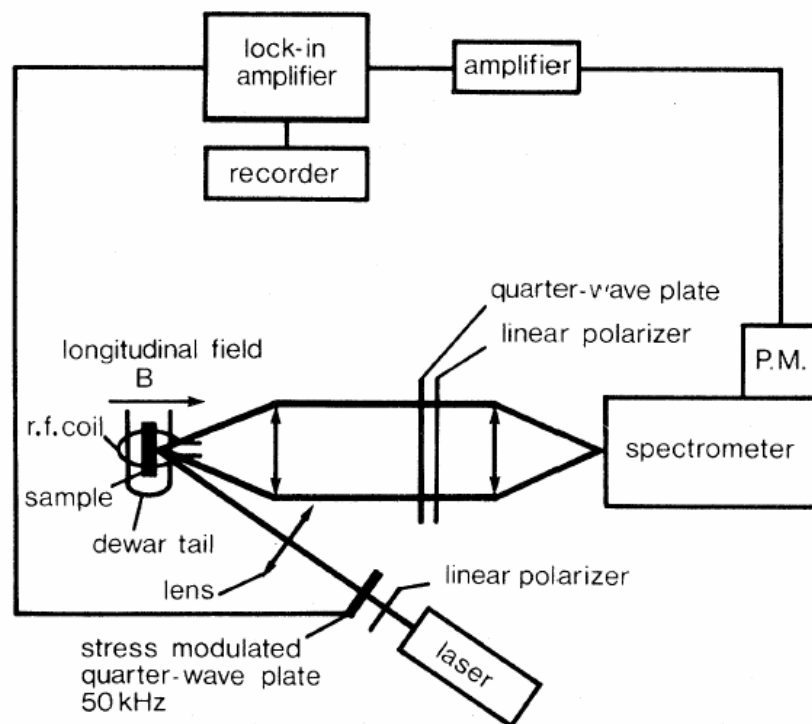


Figure 2.2 : Experimental setup for OD-ESR type experiments [23]

Electron Spin Resonance (ESR) is a very useful tool to investigate the nature and dynamics of electrons in different systems by measuring the g -factor. The g -factor value can differ considerably from 2 (for free electrons), e.g., in semiconductors where there can be strong spin-orbit interactions. The ESR condition is given by the

following equation:

$$\hbar\omega = g\mu_B B_{ext}, \quad (2.2)$$

where μ_B is Bohr-magneton. The linewidth of the resonance peak gives us important parameters

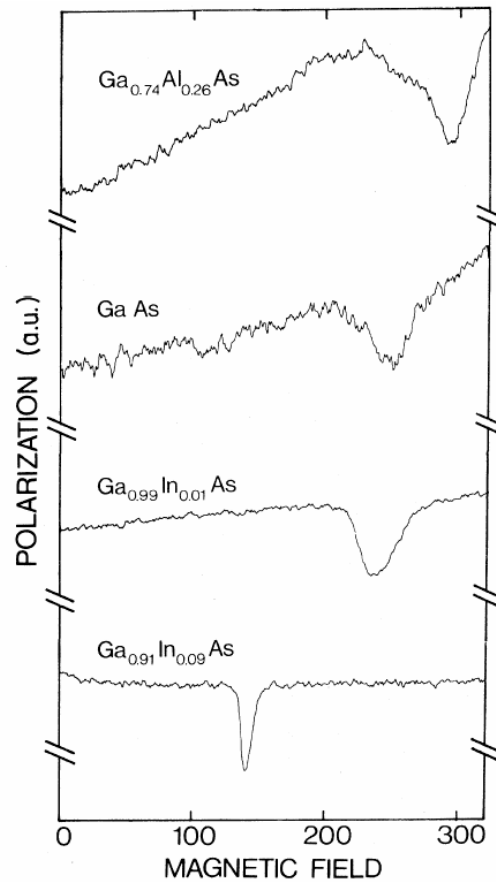


Figure 2.3 : Optically detected ESR lines for GaAs, $\text{Ga}_{1-x}\text{In}_x\text{As}$ and $\text{Ga}_{1-x}\text{Al}_x\text{As}$ at 1.7K (field in gauss, rf frequency 151 MHz) [23]

ODESR involves the creation of population differences between the Zeeman levels of the conduction electrons by pumping with circularly polarized light near the bandgap energy. The resulting electronic polarization produces in turn an emis-

sion polarization and so resonance can be detected as a change in emission polarization. Fig. 2.3 displays some typical resonance curves for GaAs, $\text{Ga}_{1-x}\text{In}_x\text{As}$ and $\text{Ga}_{1-x}\text{Al}_x\text{As}$ at 1.7K.

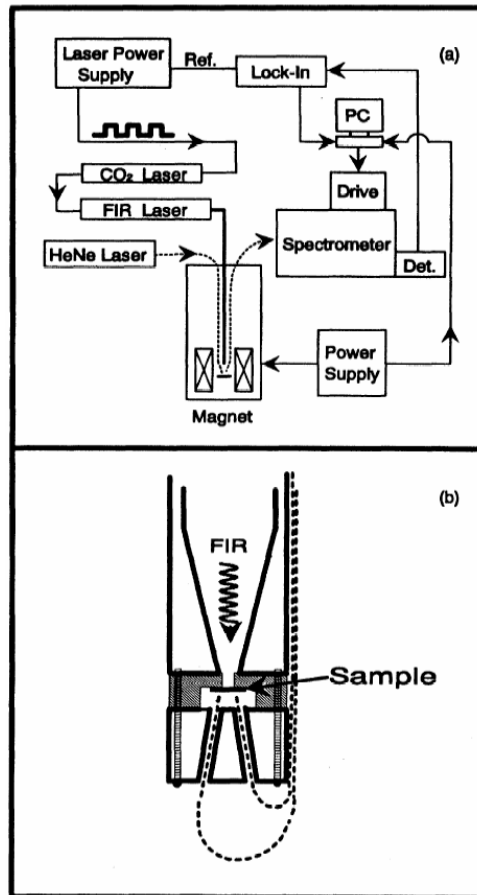


Figure 2.4 : Experimental setup for FIR-ODCR type experiments [20]

With the application of a magnetic field, energy levels of free carriers in semiconductors are quantized into Landau levels separated by $\hbar\omega_c$. Cyclotron resonance (CR) is a method for measuring the effective masses m^* of charge carriers in solids.

The condition for cyclotron resonance is given by the following equation:

$$\hbar\omega = eB/m^* \quad (2.3)$$

As a secondary purpose, one can also use CR to study carrier scattering phenomena in solids by examining the scattering lifetime τ , which can be known from the linewidth of CR peaks. Fig. 2.4 shows the experimental setup for ODCR type experiments.

This technique is similar to ODMR and ODESr involving the microwave/FIR induced change in the luminescence intensity, though in ODMR/ODESR these changes are due to spin-dependent transitions. The mechanism which results in the changes in the emission intensity at cyclotron resonance has been discussed widely. Romestain and Weisbuch [8] attributed ODCR to carrier heating at resonance since they suggested that there is a very efficient transfer between the free carriers and the excitons. Subsequent results of Cavenett and Pakulis in GaAs/AlGaAs QWs [11] are consistent with this suggestion, since they observed increases and decreases in the quantum well emission at resonance resulting from the ionisation of the bound excitons. The free (e-hh) exciton emission increased while the bound (D^0 , X) decreased.

The “heating” picture is valid only in the low magnetic field semi-classical regime, where Landau quantization is not significant. In the high magnetic field, quantum regime, CR and ESR are both quantum transitions, the former originating from orbital quantization and the latter from spin quantization. Hence there is no intrinsic difference between the techniques of ODESr and ODCR.

Many optical transitions in semiconductors involve impurity states, which serve as local centers for binding carriers. For example, a typical photoluminescence spectrum from semiconductors involves free excitons, bound excitons, band-to-impurity, impurity-to-band, and impurity-impurity (donor-acceptor) recombination lines. In the FIR, in most semiconductors neutral donor $1s \rightarrow 2p_+$ transitions and singlet/triplet

transitions of negative donor ions occur. The important thing is to select the right emission line to see a particular transition. It is also possible to obtain information about recombination mechanisms and the interactions that give rise to the various lines.

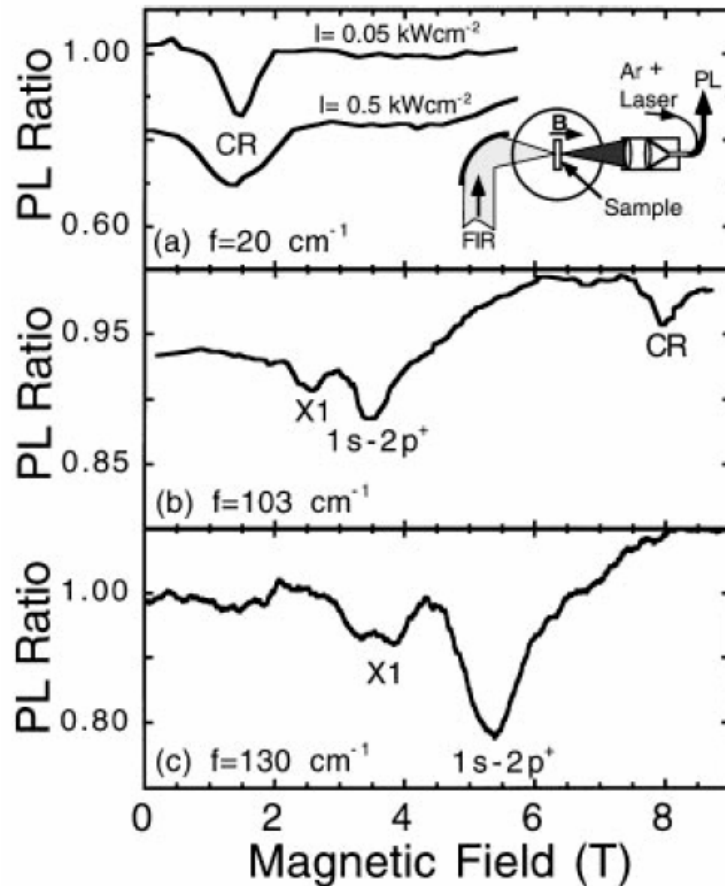


Figure 2.5 : Optically detected CR and exciton resonance (ER) lines. The ratio of the PL amplitude with and without FIR irradiation for GaAs/AlGaAs quantum wells [21]

The Coulomb interaction between electrons and holes in the semiconductors results in formation of hydrogen-like complexes known as excitons. Excitons have en-

ergy spectra similar to that of the hydrogen atom except that the energy scale is greatly reduced by the small effective electron and hole masses and the large dielectric constant of semiconductors such as GaAs. Thus, the internal energies of the transitions among the various excitonic levels all lie in the FIR region of the energy spectrum.

Fig. 2.5 plots the ratio of the PL amplitudes with and without the FIR irradiation as a function of the magnetic field. The dominant resonances are assigned to FIR-induced electron cyclotron resonance and $1s \rightarrow 2p_+$ excitonic transitions. The weaker resonances (X1) at magnetic fields below the $1s \rightarrow 2p_+$ transition is conjectured to be an excitonic feature as well, e.g., $1s \rightarrow 3p_+$. The inset in (a) shows a schematic of the experimental setup [21].

In Fig. 2.6 the solid symbols show the energy of the various FIR resonances as a function of magnetic field in GaAs/AlGaAs quantum wells [21]. The excitonic transitions such as the $1s \rightarrow 2p_+$ (solid circles) and higher energy transitions (solid triangles) can be seen in addition to the free-electron cyclotron resonance (solid diamonds). The thick solid line and thin dotted line represent calculations using excitonic theory, while the dashed lines are calculated using donor theory. The thin solid line is free-electron CR with an effective mass of $0.073m_0$. The $1s - 2s$ energy spacing of the heavy-hole exciton (large empty circles) was deduced from interband photoluminescence excitation measurements. The inset shows the magnetic field at which $1s \rightarrow 2p_+$ exciton transition occurs at two FIR frequencies in four QWs [21]

Other kinds of THz resonance that can be optically detected are polaron resonance, magnon resonance, inter-sub band resonance, ferromagnetic resonance, etc.

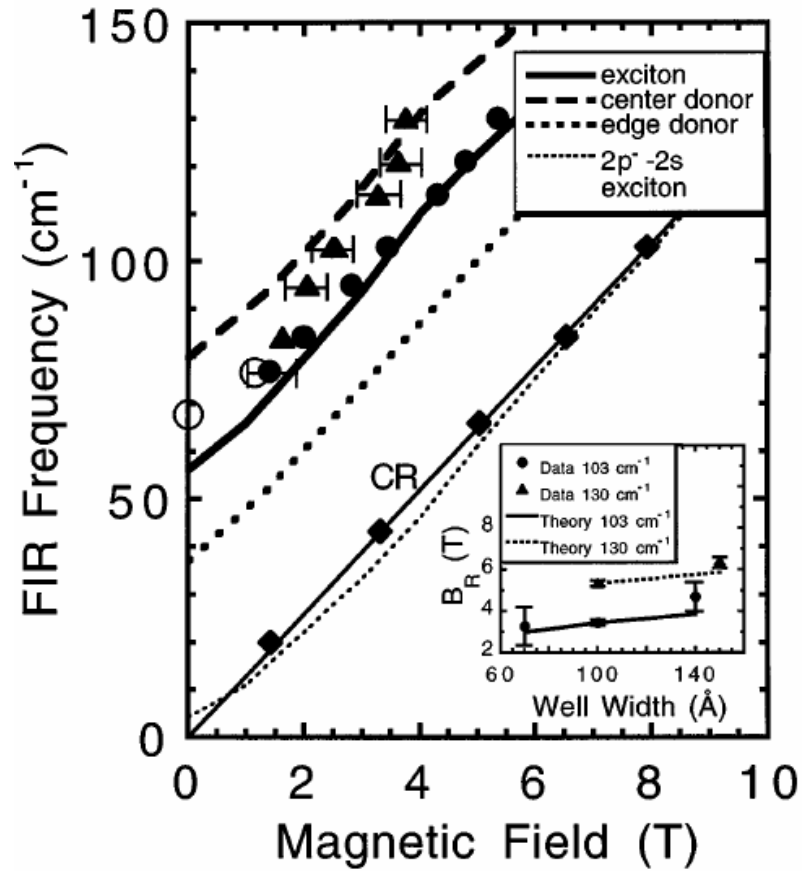


Figure 2.6 : Comparison of the experimental results to the calculations of the energy of various FIR resonances in GaAs/AlGaAs quantum wells as a function of magnetic field [21]

Chapter 3

Terahertz Quantum Cascade Lasers

3.1 The Terahertz Gap

The THz frequencies are amongst the most underdeveloped in the electromagnetic spectrum. Until recently, the slow progress in this area was primarily due to the lack of coherent solid-state THz sources that could provide high radiation intensities (greater than 1 mW) and continuous wave (CW) operations. The sources available for this region were usually weak or bulky and expensive.

This is due to the fact that the THz frequency range lies between two other frequency ranges in which conventional semiconductor devices have been well developed. On one side there is the microwave and millimetre-wave frequency range, and on the other is the near-infrared and optical frequency range.

If we approach from the low-energy side we have semiconductor electronic devices (such as transistors, Gunn oscillators, Schottky-diode frequency multipliers, and photomixers) that use freely moving electrons to generate radiation. They are limited by transit time and parasitic RC time constants. As a consequence of this, the power level of these devices decreases as $1/f^4$, or faster, as the frequency f increases above 1 THz.

On the other hand, photonic or quantum electronic devices (like laser diodes) generate radiation by oscillating bound electrons. Consequently, they are not limited by the transit time or the RC time constant. However, conventional laser diodes are limited to frequencies that correspond to the semiconductor band-gap, which is

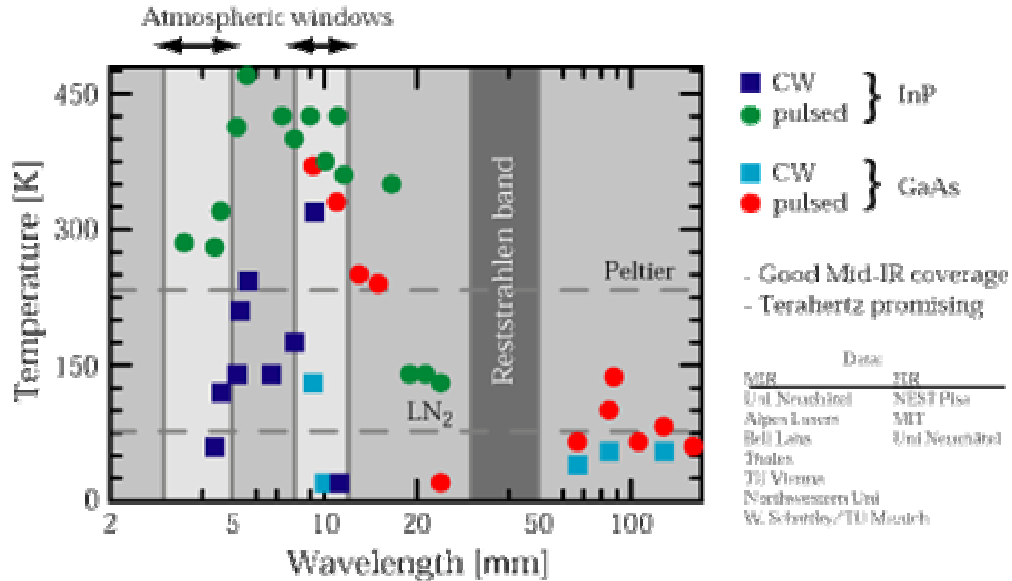


Figure 3.1 : Present QCL operation ranges (<http://www.unine.ch/phys/meso/>)

higher than 10 THz even for narrow-gap lead-salt materials. As a result, radiation in the frequency range below 10 THz is not possible for conventional semiconductor laser diodes.

3.2 Quantum Cascade Lasers

Semiconductor quantum wells are quantum-mechanical systems in which the energy levels can be designed and engineered to any value. Lasers based on intersubband transitions were proposed for long wavelength sources in early the 1970s [24]. However, due to the challenges in epitaxial material growth and the unfavorable fast non-radiative relaxation rate, there was very little progress. The first intersubband-transition lasers, also known as quantum cascade lasers (QCLs), at $4.3 \mu\text{m}$ wavelength were developed at Bell Laboratories in 1994 [25].

Since then, the QCL performance has improved substantially. Presently, QCLs are capable of emission wavelength range from 3.5 to 100 μm , peak power levels in the Watt range and above-room-temperature pulsed operation for mid-infrared (MIR) lasers [26, 27]. Fig. 3.1 shows the range of wavelengths available in present technology for QCLs.

QCLs are essentially semiconductor injection lasers base on intersubband transitions in a multiple-quantum-well (QW) heterostructure, designed by means of band-structure engineering and grown by molecular beam epitaxy (MBE). The advantages of such a scheme are evident. The emission wavelength is a function of QW thickness. Due to this reason, one can choose reliable and well understood semiconductor systems for generation of light in a wavelength range, independent of material's energy bandgap. Secondly, since this process is like a cascade, multiple photons are generated per electron, as the electron remains in the conduction band throughout the transversal of the active region. This cascading process provides the intrinsic high-power capability of these lasers. Finally, intersubband transitions are characterized through an ultrafast carrier dynamics and the absence of the linewidth enhancement factor, with both features being expected to have significant impact on laser performance.

3.2.1 Operation

As mentioned previously, QCLs are based on intersubband transitions between quantized states in multiple-QW heterostructures. Population inversion, which leads to laser action, is achieved between states within one band of a semiconductor by means of “band-structure engineering” [26]. This means that QW and barrier thicknesses and band-offsets are designed and engineered to tailor the fundamental properties of energy levels, carrier scattering rates, optical dipole matrix elements and tunneling

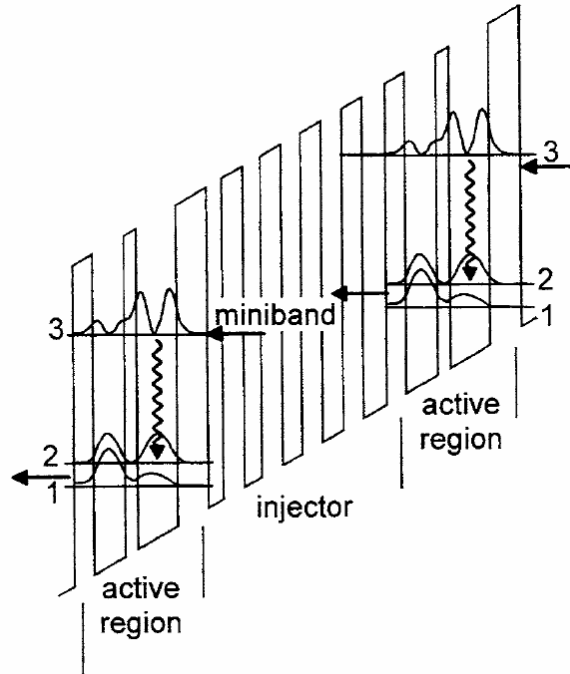


Figure 3.2 : Schematic conduction band energy diagram of two QCL active regions with intermediate injector region [26]

times within the given fundamental limits so as to optimise the population densities and transition probabilities for the various energy states. The designed structures are grown by MBE, requiring control for layer thicknesses between 0.5 to 10 nm, and through a total of 500-1000 subsequent grown layers.

Fig. 3.2 shows the schematic conduction band energy diagram of a QCL. Two active regions consisting of the QW and the barrier regions that supports the electronic states, between which the laser transition takes place with the intermediate injector region. The linear slope of the electronic potential is due to an applied external electric field. Solutions to Schrödinger's equation for this potential give the energy levels drawn and the moduli squared of the wavefunctions. The figure shows the most interesting, first three confined states (labeled 1, 2 and 3) of each active region. The

laser transition is indicated by the wavy arrows, and the electron flow by the straight arrows.

Extrinsic electrons are supplied to the injector region through doping with silicon to a sheet density of typically $1\text{-}5 \times 10^{11} \text{ cm}^{-2}$ per period of active region and injector. This typically translates to a bulk doping level of $3\text{-}5 \times 10^{16} \text{ cm}^{-3}$ [26]. This low carrier density justifies the solution of Schrödinger's equation using the QW and external bias potential while neglecting an additional potential resulting from the ionised donors and extrinsic electrons.

In this particular example, the QW thicknesses in the active region were 6.0 and 4.7 nm, and the thickness of the intermediate barrier was 1.6 nm. This results in energy separation between levels 3 and 2 of 207 meV corresponding to an emission wavelength of about $6.0 \mu\text{m}$. The energy between levels 2 and 1 of 37 meV is chosen to be close to the energy of LO phonon modes of the InGaAs/AlInAs/active region materials [26].

The scattering times are calculated using a Fröhlich interaction model, of $\tau_{32} = 2.2 \text{ ps}$ and $\tau_{31} = 2.1 \text{ ps}$. This results in a total upper state lifetime of $\tau_3 = 1.1 \text{ ps}$. Scattering time between levels 2, the lower laser state, and level 1 is $\tau_2 = 0.3 \text{ ps}$. This scattering time is very small due to the resonant nature of this transition with the LO phonon. Since $\tau_3 \gg \tau_2$, population inversion can occur between the laser levels 3 and 2 and laser action is possible. Electrons need to be supplied fast enough into level 3, by tunneling from the preceding injector region, and should exit from levels 2 and 1 into the following downstream injector region at a high rate by tunneling. Inside the injector region, electrons gain in energy due to the externally applied electric field and are injected into the following downstream active region. Typically, QCLs have a cascade containing 20-30 active regions alternated with injector regions [26].

3.3 Terahertz Quantum Cascade Lasers

Original proposals for the intersubband lasers had assumed that achieving a lasing threshold for FIR would be easier than for MIR because of the absence of optical-phonon emission at low energies. The longer upper-state lifetime would lead to lower threshold-current densities. However, detailed studies into the operation of QCLs have shown that the optical-phonon process is essential to their successful design. Resonant optical-phonon emission is used in many designs to reduce the lower state lifetime. Even in designs in which it is not directly used to engineer the upper- and lower-state lifetimes, optical-phonon emission is the dominant electron-cooling mechanism.

The development of THz QCL has turned out to be more challenging than initially expected due to two major factors. First, the energy-level separations that correspond to the THz frequencies are very narrow (~ 10 meV). As a result, the selective depopulation mechanism based on energy-sensitive LO-phonon (36 meV) scattering, which has been successfully implemented in MIR QCLs, is not applicable. Second, mode confinement is difficult to achieve at THz frequencies. Conventional dielectric-waveguide confinement is not applicable because the evanescent field penetration, which is proportional to the wavelength and is of the order of several micrometres, is much greater than the active gain medium of several micrometres.

In the FIR, intersubband electroluminescence experiments have shown that electron-electron scattering is the main scattering mechanism in clean structures at low temperatures [28]. Electron-electron scattering does not, by itself, lower the energy of an ensemble of electrons, but tends to equilibrate the population between subbands. As a result, the achievement of population inversion is even more challenging in the FIR than in the MIR.

3.3.1 Chirped Superlattice Structures Based QCLs

The first THz QCL operating at 4.4 THz was developed in 2002 [1]. This laser was based on chirped superlattice structures that have been successfully developed at mid-infrared frequencies. Active regions based on chirped superlattices are promising candidates for long-wavelength operations because the population-inversion mechanism is based on a phase-space argument and not specifically on optical-phonon emission. Mode confinement in this THz QCL was achieved using a double-surface plasmon waveguide grown on a semi-insulating (SI) GaAs substrate.

Fig. 3.3 shows the conduction band structure of a chirped superlattice design. One repeat unit in the structure comprises seven GaAs quantum wells separated by $\text{Al}_{0.15}\text{Ga}_{0.85}\text{As}$ barriers, with active region consisting of three closely coupled quantum wells. Relaxation/injection region comprises of the remaining four quantum wells. A self-consistent calculation of the conduction band structure of a portion of the layer stack in a waveguide core under a field of 3.5 kV cm^{-1} is shown. The moduli squared of the wavefunctions are shown, with miniband regions represented by shaded areas. The optical transition takes place across the 18-meV-wide minigap between the second and first miniband (states 2 and 1) and, being vertical in real space, presents a large dipole matrix element of 7.8 nm. Carriers are injected into state 2 via resonant tunnelling from the injector ground state labeled g. The second panel shows the calculated population inversion between states 2 and 1 of the active superlattice (circles), expressed in terms of electron sheet density (n_2 and n_1 respectively), and current density traversing the structure (diamonds). Both are computed as a function of bias field at 10 K

In the active regions for chirped superlattices, the upper- and lower-state wavefunctions extend over three coupled quantum wells. ‘Chirping’ the quantum well and

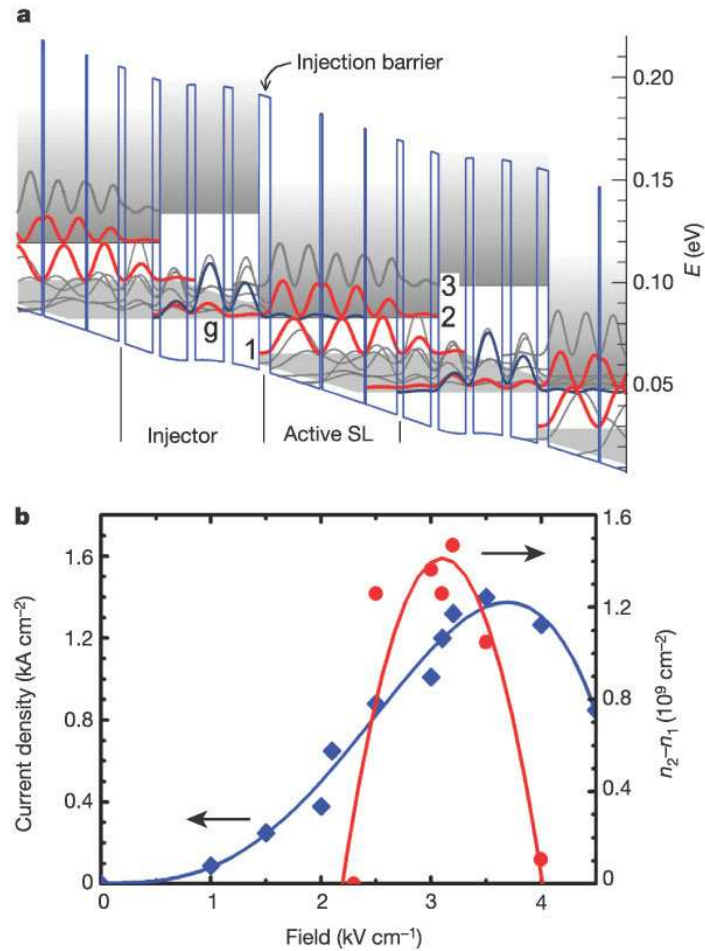


Figure 3.3 : (a) Chirped superlattice design (b) calculated population inversion and current density [1]

barrier thickness restores the large dipole matrix element existing between the states at the edge of the minigap. Depopulation of the lower lasing level depends on resonant tunneling and electron-electron scattering. The main limitations in slope efficiency and maximum operating temperatures are attributed to a thermal backfilling due to the narrow subband separations within the minibands of the superlattice and a weak population inversion.

3.3.2 Resonant Phonon Scattering Based QCLs

Recently a QCL that did use the optical-phonon scattering mechanism as a key process to achieve population inversion was demonstrated [29]. Fast LO-phonon scattering is used to depopulate the lower radiative level, and double-sided metal waveguides was used for THz mode confinement.

The direct use of LO-phonon scattering for depopulating the lower state has many advantages. When the collector state is separated from the lower lasing level by at least the LO-phonon energy, depopulation is extremely fast, and it does not depend on the temperature or the electron distribution. Secondly, the large energy separation provides intrinsic protection against thermal backfilling of the lower radiative state. Both these properties are important for higher temperature operation. This laser has demonstrated high temperature operation, at the cost of a larger threshold-current density caused by shorter lifetimes.

3.3.3 Bound-to-Continuum Transition Based QCLs

An alternate QCL scheme has been implemented based on a bound-to-continuum transition emitting $\lambda \simeq 86 \mu\text{m}$ (3.5 THz) [30]. In this design, electrons are injected in an isolated state created inside a minigap by a thin well adjacent to the injection barrier, while electron extraction occurs through a lower miniband. Due to the diagonal nature of the laser excitation, both injection efficiency and lifetime ratio (upper to lower state) are maximized, while miniband transport is employed as an efficient mechanism to minimize the lower state population. Long wavelength ($\lambda \sim 16 \mu\text{m}$), high performance QCLs based on this design concept, operating at room temperature have been demonstrated [31]. This combination of long lifetime, good injection efficiency of the upper state and good extraction efficiency of the lower state is especially advantageous in the THz QCLs where population inversion is difficult to achieve.

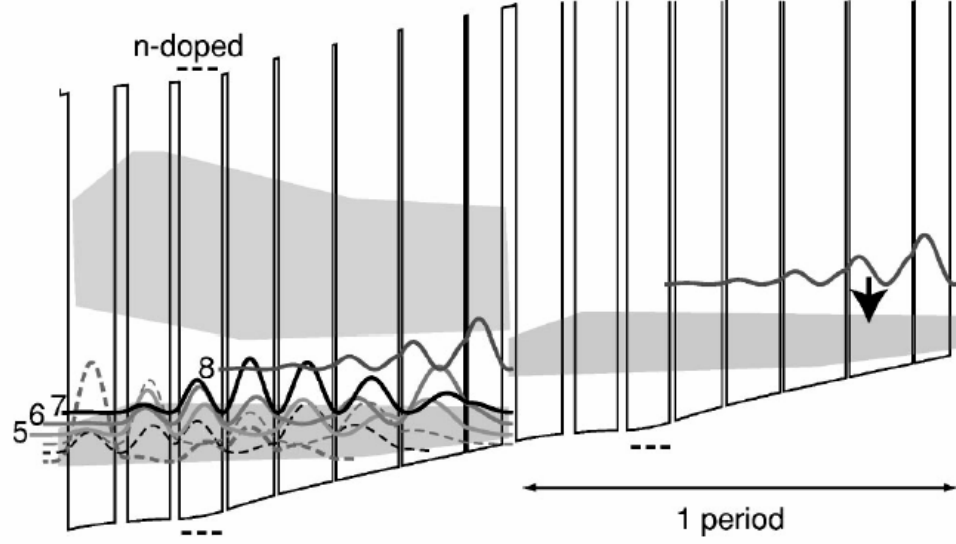


Figure 3.4 : (a) Bound-to-continuum type QCL conduction band profile [30]

The band structure of such a laser, emitting at $\lambda \simeq 86 \mu\text{m}$ is shown in fig. 3.4. The conduction band profile is computed at $T = 40 \text{ K}$ of one stage of the structure under an average applied field of 2.55 kV cm^{-1} . The GaAs/ $\text{Al}_{0.15}\text{Ga}_{0.85}\text{As}$ bound-to-continuum layer sequence of one period of the active layers starting from the injection barrier. The radiative transition occurs between $n = 8$, isolated in the minigap, and a group of three states $n = 7, 6$ and 5 . Because of level broadening caused by interface roughness and impurities, it has not been possible to identify these states individually in the intersubband luminescence or magnet-transport measurements.

3.4 THz QCLs in Magnetic Field

A QCL in a magnetic field provides an interesting system for study involving an interplay of intersubband physics and Landau level physics. As a result, there are a

number of studies done on this topic. Below I review the literature in this area. Since we are using the QCL in a magnetic field, it is necessary to understand how their performance changes with magnetic fields.

On applying a magnetic field parallel to the degrees of freedom of the two-dimensional (2D) electronic system, in this case a quantum well heterostructure, the magnetic potential adds to the electronic potential of the quantum wells. This effect results in the breakdown of the carefully engineered energy levels in the QCL. Since the QCL consists of a succession of quantum wells, changes in the energy levels in all of these will substantially modify the recombination and injection processes, hence no lasing action can be observed.

When an intense magnetic field is applied perpendicularly to the degrees of freedom of a 2D electronic system, its energy spectrum changes completely. The continuum of states in the plane is broken by magnetic confinement into a series of discrete levels also known as Landau quantization. It has been shown the the breaking of a 2D system into ladders of 0D states modifies the the lifetime of the excited energy levels [32]. In spite of these modifications, lasing action has been observed for QCLs in this magnetic field configuration. Since our ODR experiment requires the use of a QCL in a magnetic field, we will be utilizing this property to mount our QCL in a way that the magnetic field is perpendicular to the 2D electron gas.

In MIR-QCLs, electrons are injected by tunneling into a two-dimensional excited state, whose lifetime is mainly controlled by the electron-longitudinal-optical phonon interaction. The energy of these optical phonons $\hbar\omega_{LO}$ in GaAs is constant. Therefore, in a system made of discrete energy levels, phonon emission is either inhibited or resonantly enhanced by the presence of levels at an energy $\hbar\omega_{LO}$ below the the excited state.

At low temperatures, the main scattering mechanisms for intersubband transitions

in the far-infrared at low temperature are electron-electron scattering and interface roughness. This is in contrast to the transitions in the MIR range, where LO phonon is the dominant scattering mechanism. A strong perpendicular magnetic field will break the in-plane dispersion of the subbands and create a ladder of Landau levels attached to each subband, which will strongly modify these scattering mechanisms by reducing the phase space.

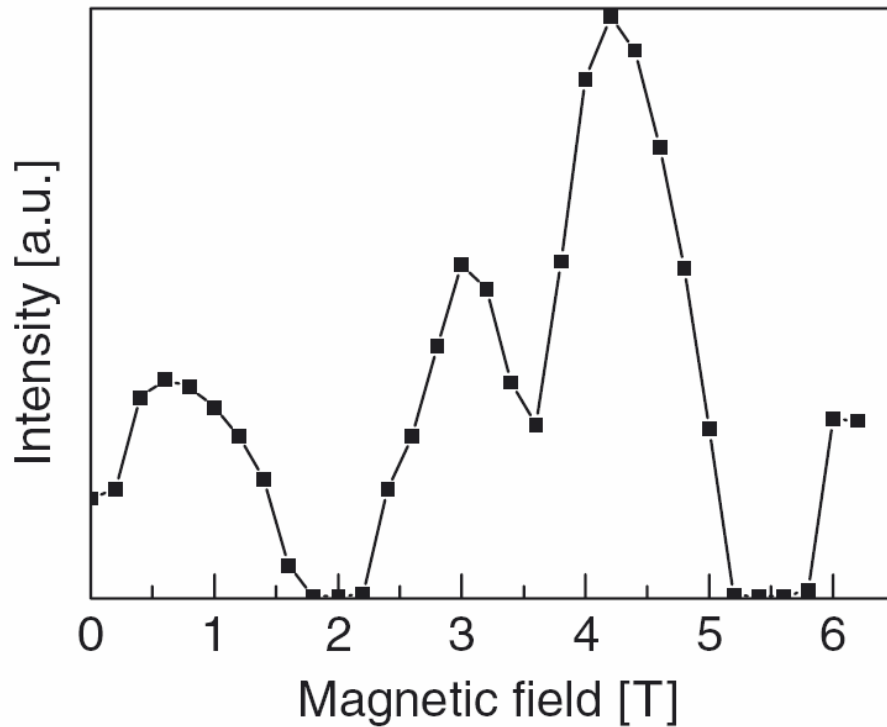


Figure 3.5 : Chirped superlattice type QCL emission intensity as a function of the magnetic field [33]

In fig. 3.5, the laser emission intensity increases for certain values of the magnetic field when compared to $B = 0$ T. The QCL used for this experiment had a chirped superlattice type structure. For increasing magnetic field, oscillations are observed.

This effect can be understood as a consequence of the discretization of the energy spectrum. In the parabolic dispersion relation (in the absence of magnetic field), the energy conservation requirement for intersubband Auger scattering processes is fulfilled for a continuum of energy changes ΔE . However, when a magnetic field is applied, the only allowed energy changes ΔE are multiples of the cyclotron energy $\hbar\omega_c$. Since the Auger-scattering rates scale inversely with the associated change in energy and momentum, it is more and more suppressed with increasing Landau-level splitting. The laser intensity is directly proportional to the inversion, which in turn is directly proportional to the injection rate and inversely proportional to the non-radiative relaxation rate.

Laser emission minima is observed where the magneto-intersubband resonance condition is met:

$$E_2 - E_1 = \hbar e B_N N / m^* \quad (3.1)$$

Here $E_2 - E_1$ is the energy difference between the lowest Landau levels of the upper and lower laser transitions, \hbar the Planck constant, e the elementary charge, B_N the magnetic flux density, m^* the effective mass, and N is an integer. Resonant tunneling between Landau levels provides an additional path for non-radiative relaxation, and this causes the reduction of the population inversion leading to a decrease in the laser emission intensity. Theoretical models have been proposed which describe the momentum transfer caused by interface roughness or impurities, which is required for resonant transfer between Landau levels of different subbands. The laser stops working at these magneto-intersubband resonances [33].

An efficient injector requires high scattering rates to achieve good injection into the upper laser state as well as fast extraction out of the lower laser state. Therefore, it is advantageous to have magneto-intersubband resonance between all the injector states, $\Delta E_{injector}$, between the last injector state and the upper laser level as well

as the lower laser state and the first extractor state. The energy difference between injector states is small ($\sim 3.1 - 3.8$ meV) and the condition for complete magnetic quantization $\hbar eB/m^* > \Delta E_{injector}$ is met at relatively low magnetic fields. Optimum performance of the laser is achieved for $\hbar eBM/m^* = \Delta E_{injector}$ and $\hbar eBN/m^* \neq \Delta E_{laser}$, where N and M are integers. The interplay between the increased injector efficiency and reduced non-radiative relaxation determines the detailed dependence of the laser intensity of the magnetic field. A red shift of the laser wavelength in the magnetic field has also been recorded. Though a conventional Stark effect can be observed in QCL type structures, it is not certain as to the origin of this shift as it represents a much “stronger” effect than Stark shift. It is conjectured that the differences in the level population are the most probable reason for the shift [33]. Non-parabolicity of energy levels in a magnetic field could also cause this shift.

Upon applying a perpendicular magnetic field to the MQW system, the free electron in-plane dispersion with energy $E_{i,k} = E_i + \hbar^2 k^2 / 2m^*$, of each of the two-dimensional states will break into a set of equidistant Landau levels separated by cyclotron energy $\hbar\omega_c = \hbar eB/m^*$. In the presence of this additional confinement, the intersubband scattering rate strongly depends on the respective energies of the Landau levels associated with the separate subbands. Because of the short-range disorder caused by interface roughness, this scattering rate will increase whenever two Landau levels with different indices associated with different subbands of energy E_i and E_j are in resonance, i.e. $\Delta E_{i,j} = \delta n \hbar\omega_c$ is satisfied for an integer δn . On the other hand, when the Landau ladders are off resonance, the scattering rate will be minimized.

One of the ways to make use of this phenomena is the control of scattering rate by additional in-plane confinement potential. This allows the design of THZ QCL structures with improved population inversion, in which the upper laser state lifetime

is increased by an off-resonance condition, while the lower state lifetime is simultaneously decreased by resonance. Since this mechanism is Fermi-level independent in a parabolic subband dispersion and will exist up to higher temperatures. This method provides a powerful way to modify selectively the lifetimes of narrow confined states. This technique can be valuable when trying to extend operating frequencies of the QCLs to the low-THz region where the photon energy is close to the natural broadening of active superlattices.

A low threshold THz laser emission ($f = 3.6$ THz) exploiting the in-plane confinement caused by a perpendicular magnetic field applied on a quantum-cascade structure has been observed [34]. The design strategy employed makes use of the selective opening and closing of relaxation channels by elastic scattering between Landau levels. The key effect is the reduction of the lower state lifetime of the lasing transition that produces the population inversion. The structure shows laser action only with applied magnetic field and yields low threshold current density.

Chapter 4

Experimental Methods

In this chapter we discuss our experimental setup to observe ODTR in semiconductor nanostructures. To highlight the versatility of our system we will also demonstrate how our setup can be used for photoluminescence (PL), magneto-optical as well as magneto-transport measurements simultaneously.

4.1 ODTR Setup

Fig. 4.1 shows the schematic of the experimental setup. Since ODTR is essentially a two-step experiment, in the first step we used an argon-ion laser in the visible range, to create photoluminescence. This excitation is sent inside the magnet through an optic fiber. The fiber has two uses, one is to carry the laser excitation to the sample, second to collect the PL signal from the sample. The THz QCL is mounted on the sample stick itself in close proximity of the sample so as to maximise the irradiation of the sample. The collected signal is collimated outside the magnet and passes through a dichroic mirror which splits the input and output paths. The signal is recorded using a spectrometer with a single channel Silicon detector and a standard lock-in method. Fig. 4.1 shows the schematic of the experimental setup.

Once the PL of the sample for different magnetic fields has been measured, the spectrometer grating is moved to the peak position of the desired feature. The modulation of the argon-ion laser is stopped, and the THz QCL is now modulated, with the modulation frequency used as the reference for the lock-in. The magnetic field

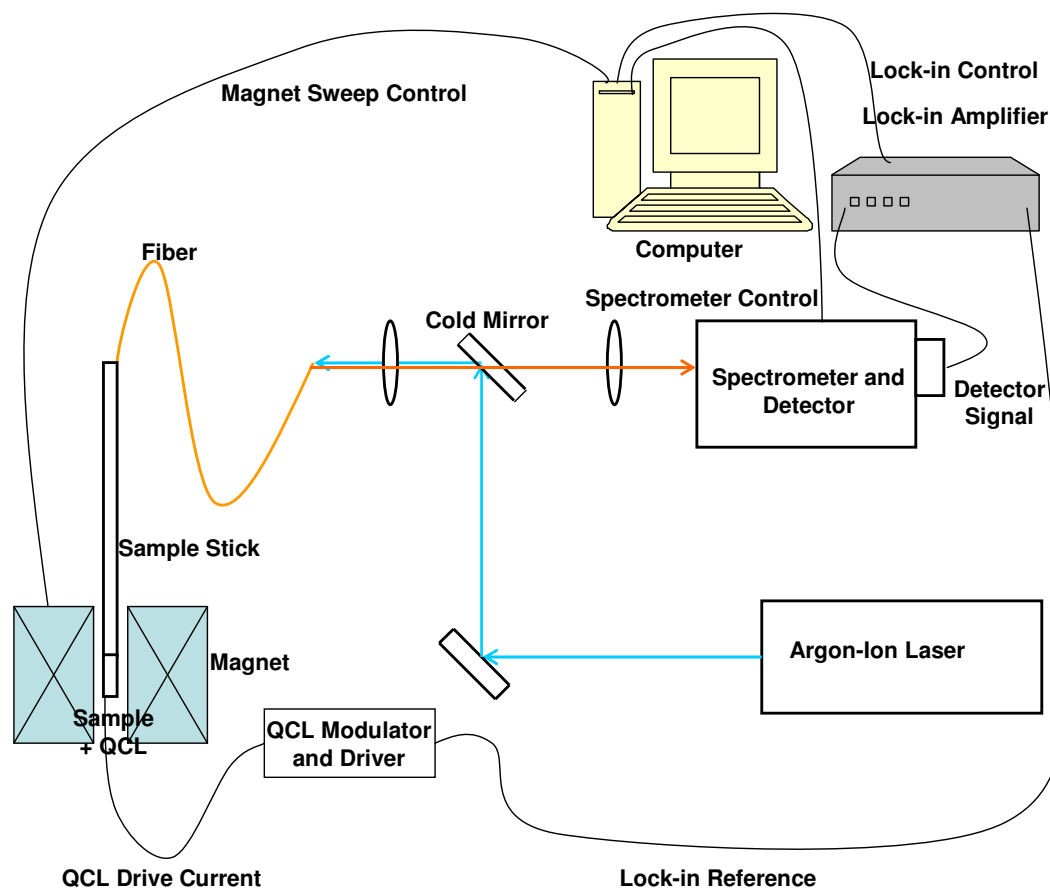


Figure 4.1 : Setup for the ODTR experiment

is swept, and the change in PL peak magnitude is measured. At resonance there is a sharp change in magnitude of the signal, which is otherwise quite flat. Since this change is expected to be about 1%, it is important that the PL signal is optimized before measuring any data.

Fig. 4.2 is a photograph of the experimental setup. As can be seen, our setup is extremely compact. In the following sections, we describe in detail the various instruments and components used in our setup.

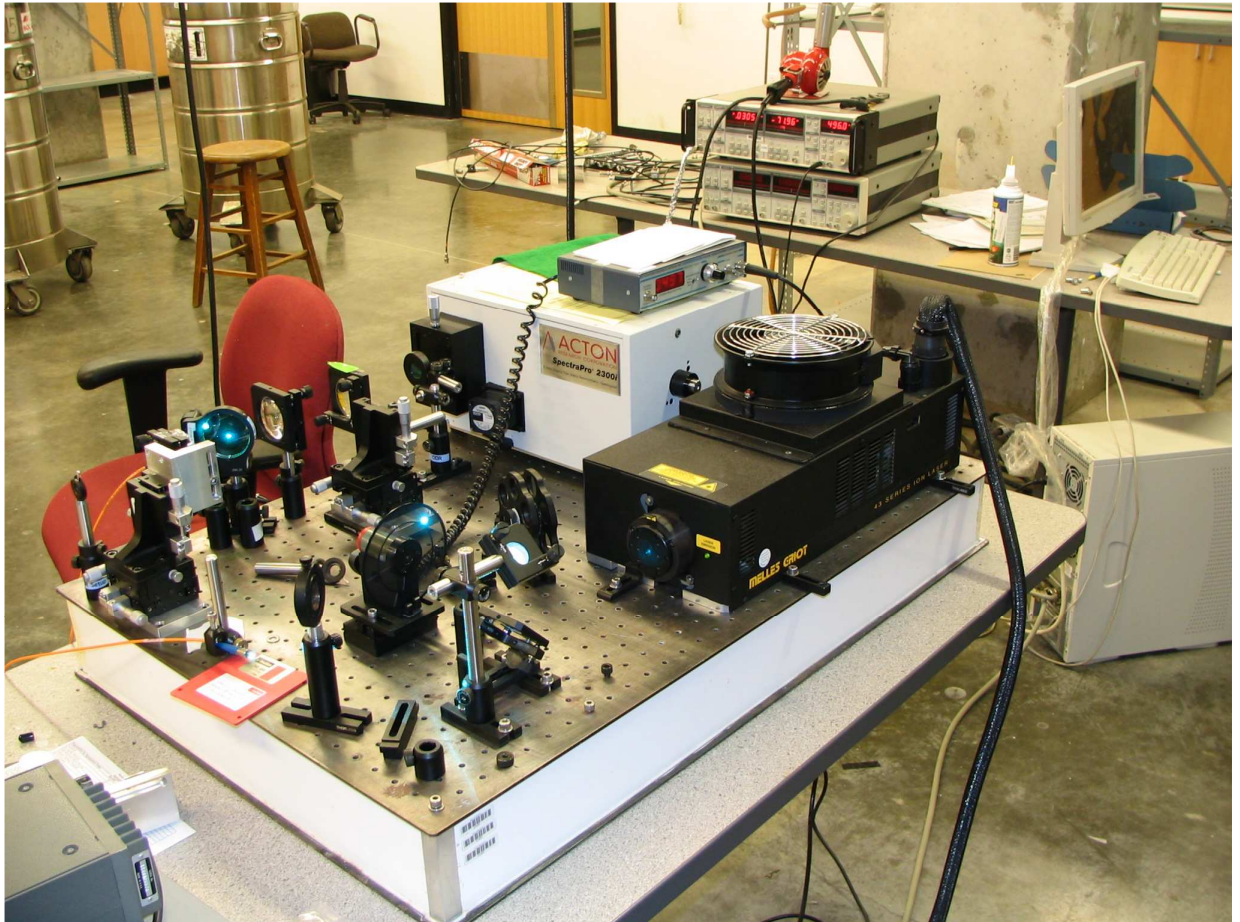


Figure 4.2 : Photo of the setup for the ODTR experiment

4.2 Lasers

4.2.1 Argon-Ion Laser

The argon-ion laser operates in the visible and ultraviolet spectral regions by utilizing an ionized species of the noble gas argon. Argon-ion lasers function in a continuous wave (CW) mode when plasma electrons within the gaseous discharge collide with the excited laser species to produce light. Argon-Ion lasers are the preferred light source in the blue-green wavelength range to provide excitation to generate photolumines-

cence. Compared to solid-state lasers or other laser technologies with similar output parameters the Argon-Ion lasers have technical advantages like high power stability, good beam quality, high beam pointing stability, low noise level, exceptionally high lifetimes and trouble free operation as well as the better price-performance ratio.

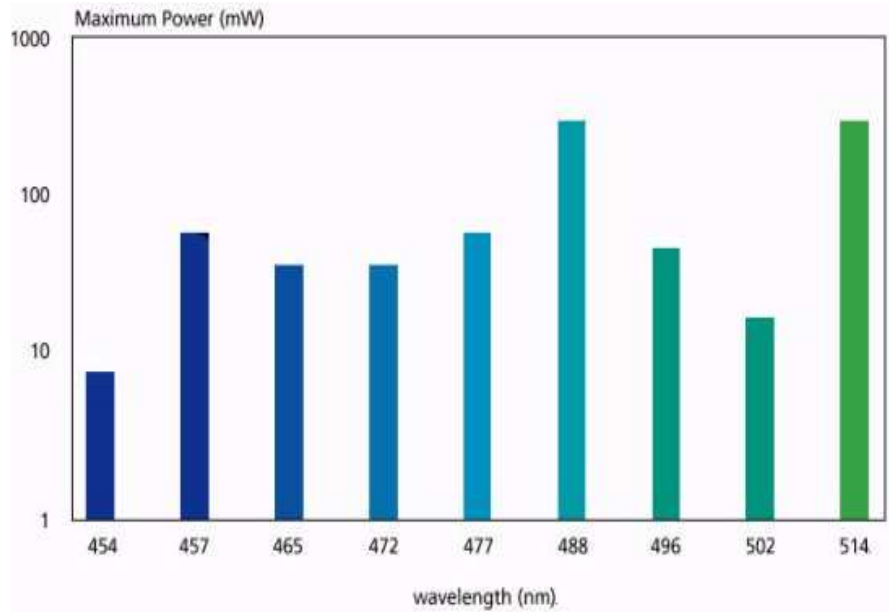


Figure 4.3 : Laser emission lines for the Argon-ion laser (<http://www.melles-griot.com>)

Argon-ion laser utilized in our experiment is a multi-line Melles Griot Series 543 air-cooled laser system. Our laser can produce a combined output power between 60 and 300 milliwatts in the blue-green spectral region with lines ranging from 454 nm to 514 nm. The strongest output is at 514 nm and 488 nm wavelengths. An integral fan is provided to air-cool the system. Fig. 4.3 shows the laser emission lines for our Argon-ion laser.

4.2.2 Quantum Cascade Laser

The THz QCLs that we have used in this experiment have been grown by the Mesoscopic physics group at the University of Neuchatel led by Professor Jerome Faist, who is one of the leading researchers in the field of QCLs.

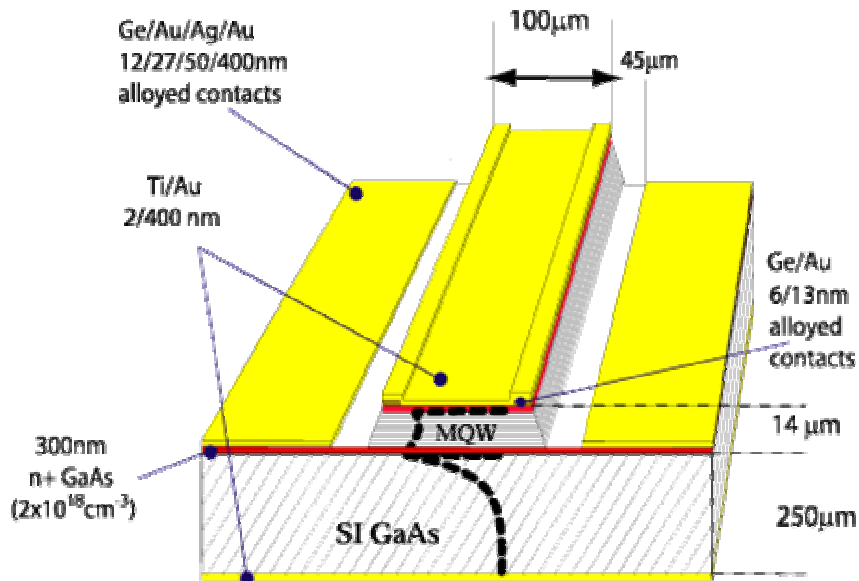


Figure 4.4 : Schematic diagram of the sample processing for a THz QCL [35]

These QCLs have an emission line at $86 \mu\text{m}$ and are capable of optimal CW operation at low temperatures ($\sim 10 - 40 \text{ K}$). The active region is based on a bound-to-continuum transition [30]. Since we will be mounting the QCL on the sample stick which will be inserted inside the magnet, we do not have to worry about cooling the QCL separately.

Fig. 4.4 shows the schematic diagram of sample processing for the THz QCL. The dashed line represents the optical mode intensity in the transverse direction.

Fig. 4.5 is a photograph of the THz QCL device that we used for our experiments.

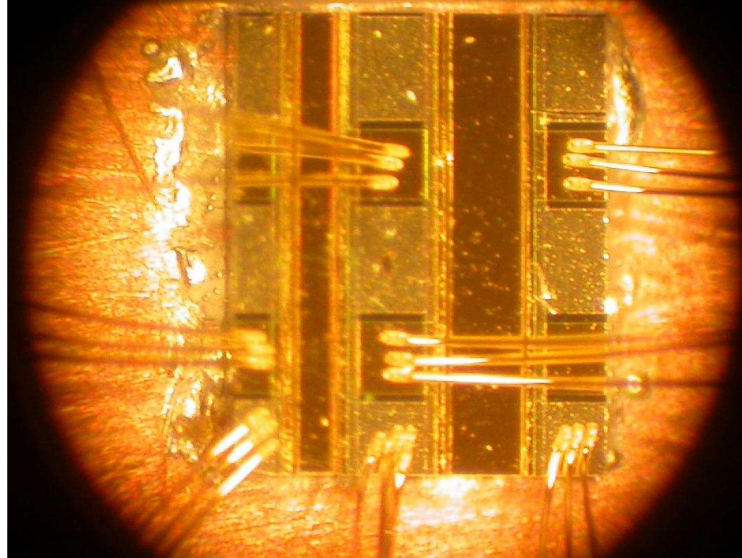


Figure 4.5 : Photograph of a QCL

It can be seen that there are two laser strips. One of the strips is 100 nm wide and the other is 200 nm wide and the length of both the strips is 1.3 mm. The optical power- and voltage-current characteristics in the pulsed mode for the 200 μm laser strip is shown in fig. 4.6. The optical power- and voltage-current characteristics in the CW mode for the 100 μm wide laser is shown in fig. 4.7.

4.3 Superconducting Magnet

A Janis “SuperVariMag” superconducting magnet system is used to provide the magnetic field. This magnet system has a rated central field of 6 Tesla (60 kilogauss). Our sample is mounted on a sample stick inside the Janis “SuperVaritemp” system, which is essentially a variable temperature insert (VTI) built into the helium reservoir of the dewar. The VTI can provide sample temperature control from 1.2 K to 300 K by

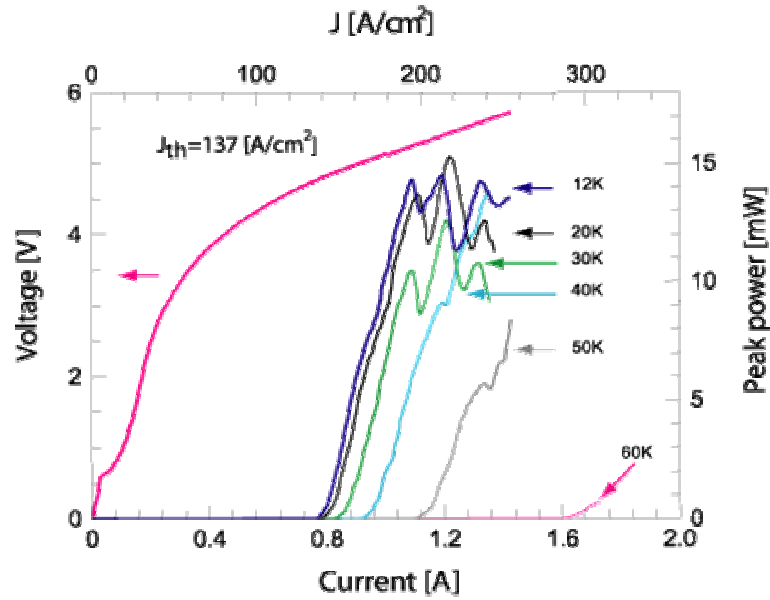


Figure 4.6 : Optical power characteristics of the QCL in pulsed mode (Jérôme Faist's group at University of Neuchatel)

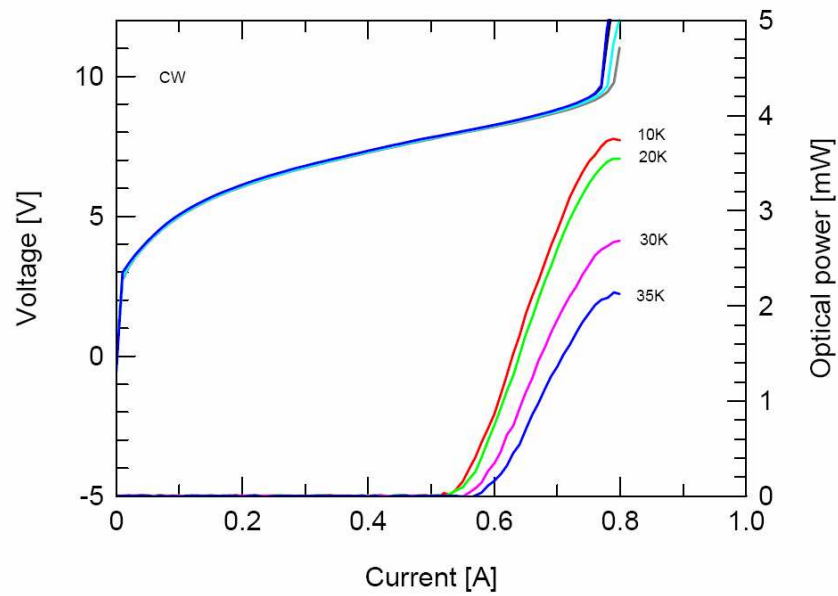


Figure 4.7 : Optical power characteristics of the QCL in CW mode (Jérôme Faist's group at University of Neuchatel)

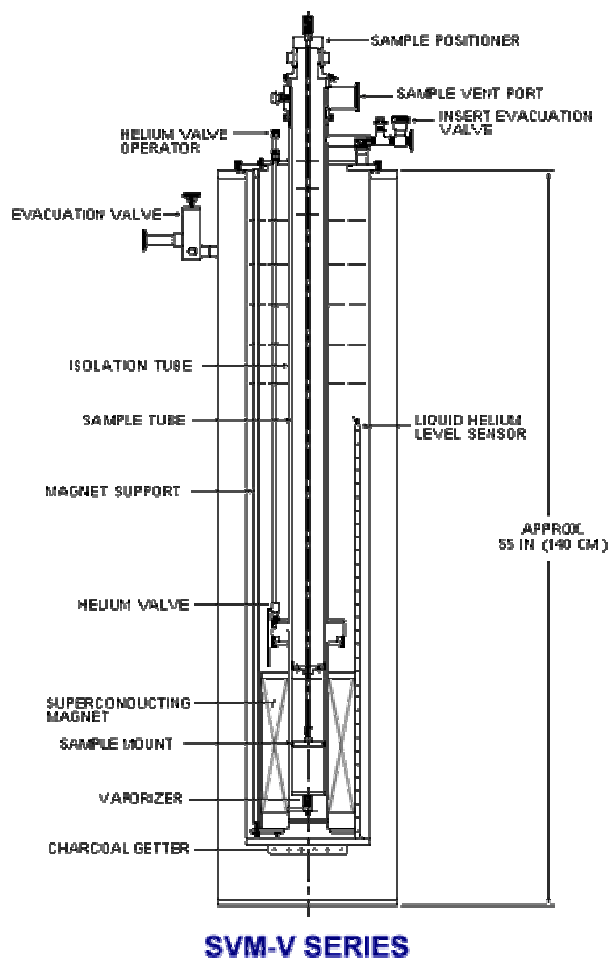


Figure 4.8 : Superconducting magnet used in our experiment (<http://www.janis.com>)

balancing Helium flow with a built-in heater. Fig. 4.8 shows the schematic diagram of the magnet used in our experiment.

4.4 Sample Stick and Holder

The sample holder for our experiment has special requirements, hence the standard sample holder for the magnet could not be used. Our sample stick is made of a

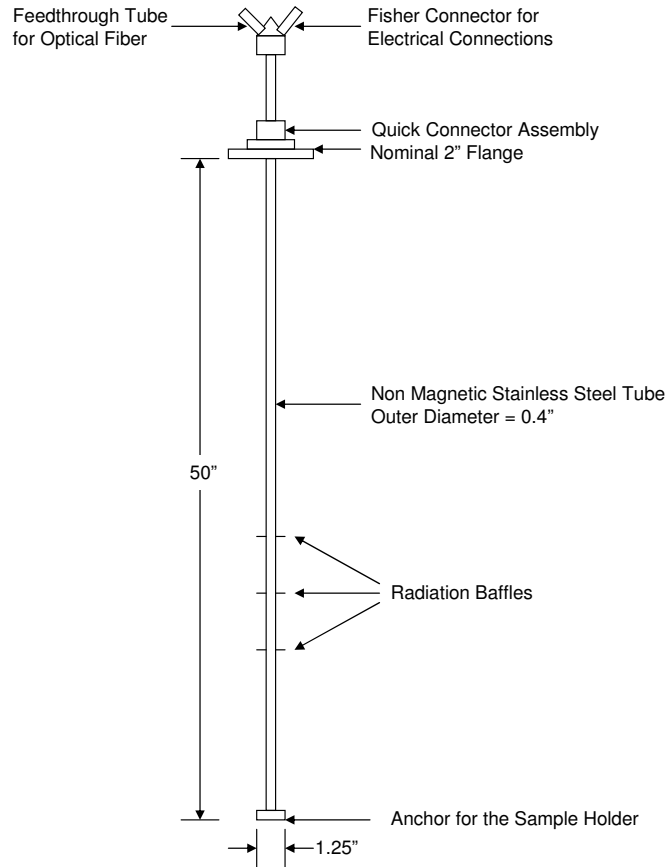


Figure 4.9 : Design of the sample stick for the ODTR experiment

hollow tubing, so as to provide a casing for the fiber. The sample stick designed has feedthrough connections for wires. This arrangement has multiple uses. One is to provide the current to the QCL from the modulated current driver outside the magnet. Secondly, it enables us to connect these wires to contacts made on the sample so as to perform transport measurements. Since we use two sets of electrical feedthroughs, we can monitor transport phenomena simultaneously with QCL operation. As a result we can perform a variety of experiments, viz., PL, ODR, photoconductivity

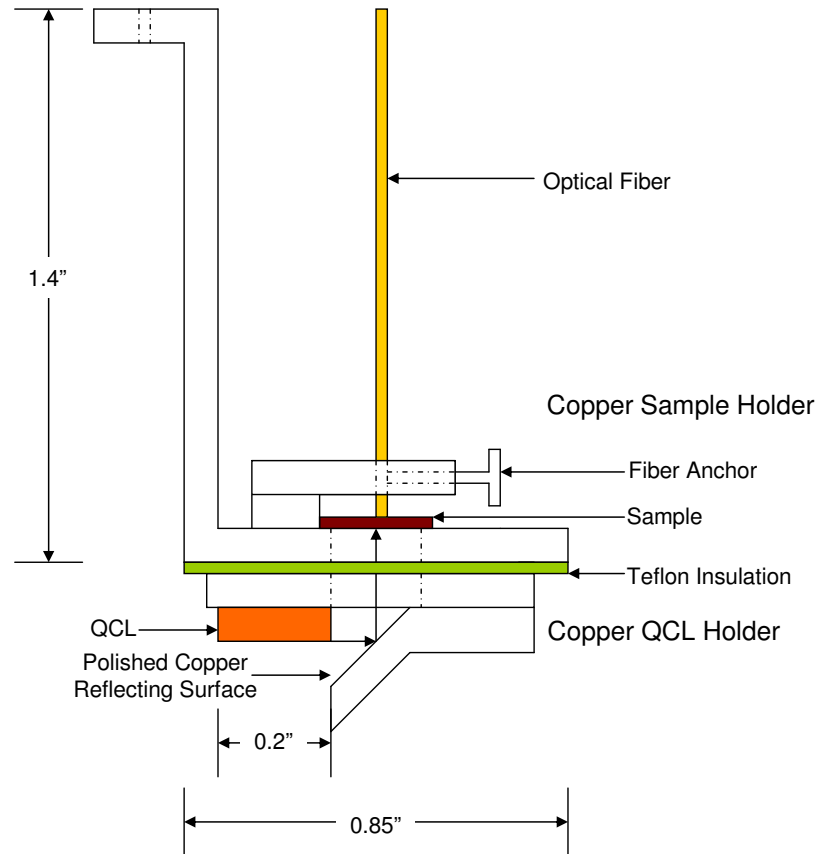


Figure 4.10 : Design of the sample holder for the ODTR experiment

and Shubnikov-de Haas on the same sample at the same time. Fig. 4.9 shows the drawing of the sample stick.

The sample holder also has to be special, as it has to hold the QCL as well as the sample in a particular configuration (growth directions parallel to the field). Due to all these considerations, we designed a sample stick ourselves. One of the unforeseen problems that cropped up due to placing the QCL on the sample stick was joule heating of the sample due to the QCL current. This problem was mitigated to an

extent by thermally isolating the QCL from the sample by means of a teflon insulator. Fig. 4.10 shows the drawing of the sample holder. Fig. 4.11 shows the photograph of the sample holder.

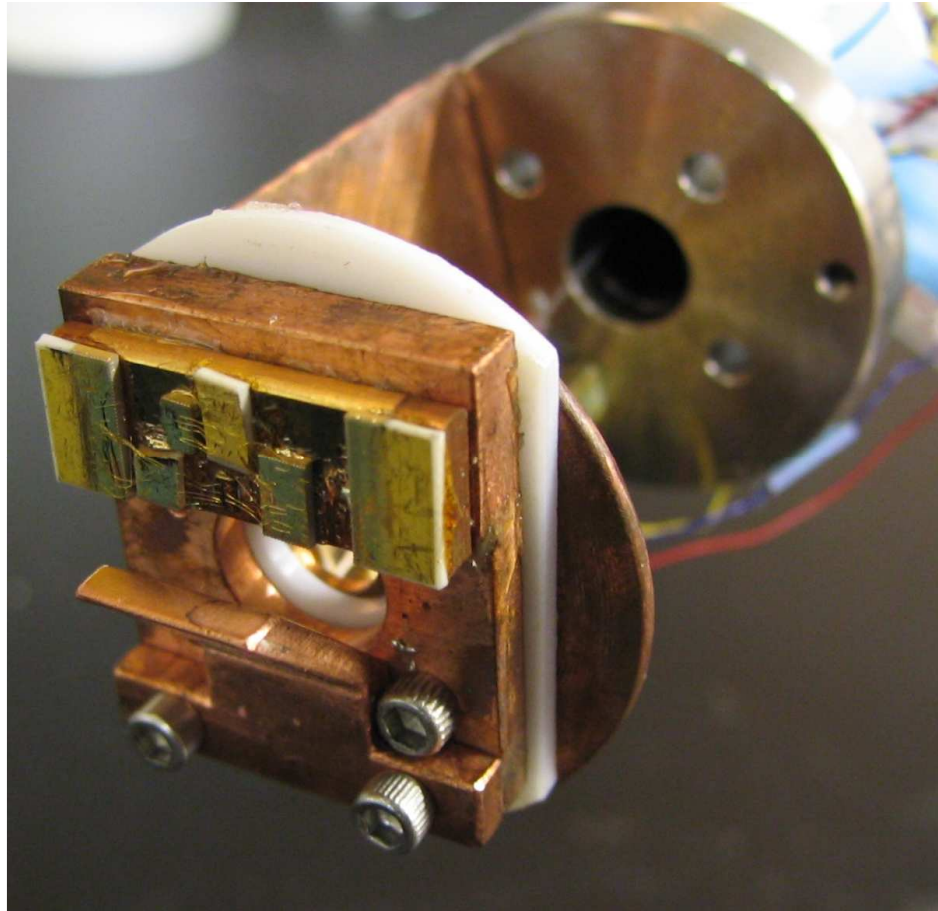


Figure 4.11 : Photo of the sample holder with the QCL for the ODTR experiment

4.5 Dichroic Mirror and Filters

To make sure that we do not allow any high wavelength argon-ion laser artifact to interfere with the PL signal, we use a 700 nm short-wave-pass filter, before the dichroic

mirror. The Dichroic mirror reflects short wavelengths (< 650 nm) and transmits long wavelengths (> 700 nm).

Since the Dichroic mirror is transparent to the PL signal, which is observed between 750 nm and 1100 nm for our samples, it goes through to the spectrometer. The dichroic mirror also serves to filter any argon-ion laser radiation that might be reflected by the sample. However it is not sufficient to remove all the argon-ion laser lines which can obliterate the PL signal. To make sure such a thing doesn't happen, we use two long wavepass filters to neutralize the laser lines.

4.6 Optical Fiber and Associated Optics

The visible beam passes through a special purpose lens assembly which, focuses the laser beam into a tight spot at the entrance of a fiber. The optical fiber used was a multimode fiber with a core diameter of 200 μm and a numerical aperture of 0.39. The good numerical aperture of the fiber allows a high collection of the PL signal from the sample.

The fiber goes all the way to the sample, touching it, so as to maximize collection efficiency. Since the fiber was going to be used in cryogenic temperatures, we had to make special nylon attachments on the sample holder to hold the fiber (without breaking it) to prevent shrinkage. The PL signal is collimated by the same special lens assembly that focuses the laser beam into the fiber.

4.7 Lock-in Detection Techniques

In the PL/ODR experiments, we adapted a lock-in amplifier (SR 830, Stanford Research System, Inc) to record the signal. This is based on a well-known phase sensitive detection technique. Essentially, a lock-in amplifier will only be sensitive to the

component of the signal which has the same frequency AND phase as the reference. External modulation from a mechanical chopper (for argon-ion laser) or power supply modulation (for the QCL) was used to provide the reference frequency to the lock-in amplifier. Through this simple method, we successfully recorded the PL/ODR signal. The detector for all the experiments was a fast (~ 1 ns) silicon detector (Thorlabs DET110), which has sufficient sensitivity to respond to the PL signal.

4.8 Samples Used

4.8.1 InGaAs/AlGaAs Multiple Quantum Well

The main sample used for our experiments was an InGaAs/AlGaAs multiple quantum well (sample 209B) sample. These samples were grown by Jim Harris' group at Stanford University. The energy band calculations for this sample are given in fig. 4.12.

4.8.2 Quantum Dots

The quantum dot (QD) sample has one layer of InAs QDs, 70 nm below the surface. The density is about 200 QDs/ μm^2 . This sample also has a layer of QDs on the surface. These samples were grown by Glenn Solomon at Stanford University.

4.8.3 Dilute Magnetic Semiconductors

The dilute magnetic semiconductor (DMS) samples are alloys of Mn with GaAs. These high-quality samples were grown by Hiroo Munekata's group at the Tokyo Institute of Technology. Fig. 4.13 shows the growth structure of this sample.

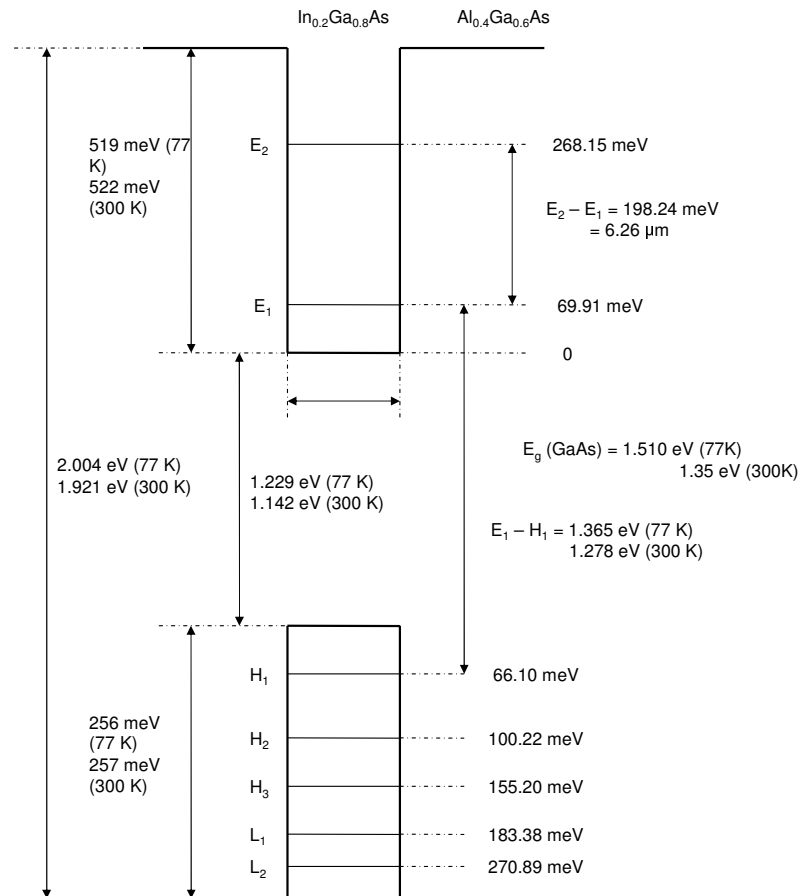


Figure 4.12 : Energy band calculations of sample 209B

$\text{Ga}_{1-x}\text{Mn}_x\text{As}$	50 nm	$x = 0.024$
GaAs	10 nm	
$\text{Ga}_{1-y}\text{In}_y\text{As}$	1000 nm	$y = 0.14 - 0.17$
HT – GaAs	300 nm	
GaAs (001)		$T_C = 30 \text{ K}$

Figure 4.13 : Structure of DMS sample T580

Chapter 5

Results and Discussion

Over the course of this experiment, we examined the magneto-PL of various samples. The most promising candidate for observing ODR as well as magneto-transport phenomena was sample 209B. In addition, we also examined the magneto-PL of other samples, notably AlGaAs/GaAs MQWs, quantum dots (QDs) and dilute magnetic semiconductor (DMS) samples. The versatility of our system in measuring magneto-optical as well as magneto-transport data allows us to measure the Shubnikov-de Haas effect in one of the samples. Finally, we obtained some preliminary ODR data by bringing together the different components.

In this chapter, we present some of the results that we obtained.

5.1 Magnetic Field Dependent PL

In Fig. 5.1 magnetic field dependent PL data for the InGaAs/AlGaAs MQWs is shown. The excitation used was a 20 mW Argon-ion laser. Temperature of the sample was 1.5 K. We used a room temperature silicon detector. The spectrometer grating used had a groove density of 1200 g/mm and a blaze wavelength of 750 nm. The input and output slits of the spectrometer were set to 500 μm . The lock-in time constant was 100 ms, with the dwell time at each frequency (controlled by the computer) set to 400 ms.

The main peak is due to the photon emitted by the free-exciton recombination. We can see a blue shift of the peak position with increasing magnetic field which is

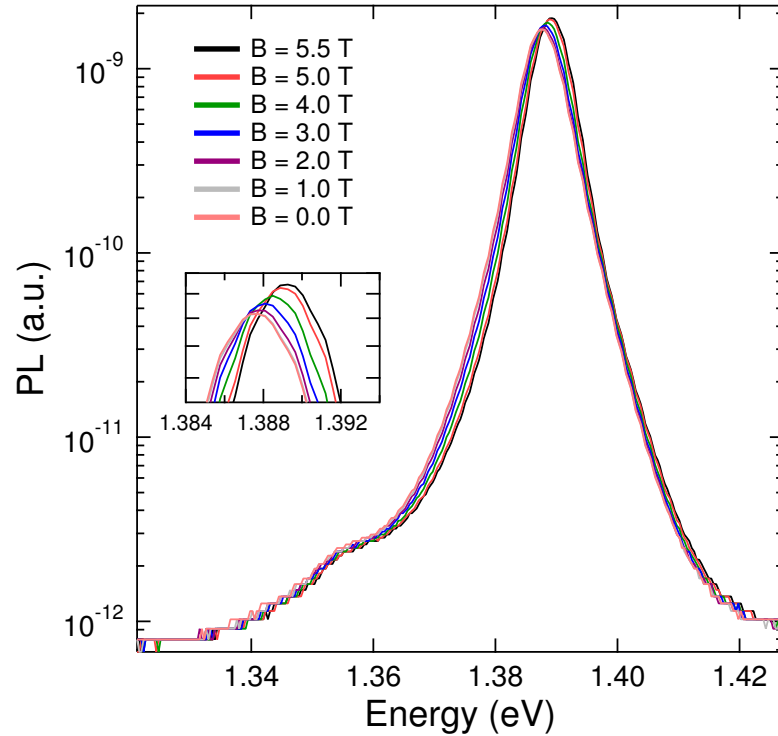


Figure 5.1 : Magnetic field dependent PL data for InGaAs/AlGaAs MQW sample.

essentially a diamagnetic shift. This can be attributed to increased confinement of carriers leading to an increase in Coulombic interaction, which becomes a dominant characteristic at high magnetic fields. .

In Fig. 5.2 magnetic field dependent PL data for the quantum dot sample M208 is shown. The excitation used was a 20 mW Argon-ion laser. Temperature of the sample was 1.5 K. We used a room temperature silicon detector. The spectrometer grating used had a groove density of 300 g/mm and a blaze wavelength of 1 μm . The input and output slits of the spectrometer were set to 500 μm . The lock-in time constant was 300 ms, with the dwell time at each frequency (controlled by the computer) set to 1000 ms.

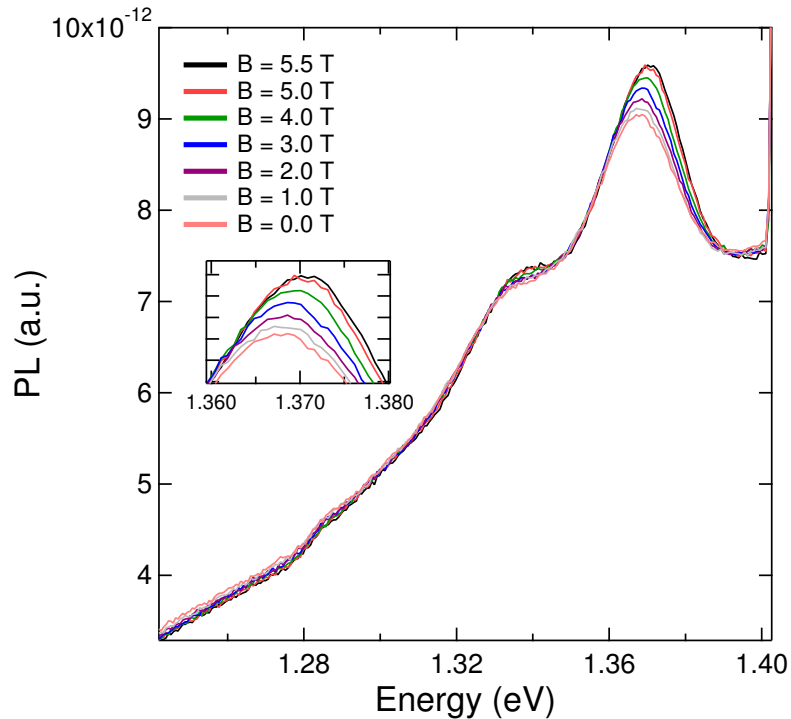


Figure 5.2 : Magnetic field dependent PL data for the quantum dot sample

The main peak in this sample is due to the ground state emission. We can see a blue shift of the peak position with increasing magnetic field which is essentially a diamagnetic shift. This can be attributed to the magnetic field induced confinement which further increases the existing confinement of carriers in the quantum dot, leading to an increase in Coulombic interaction.

In Fig. 5.3 magnetic field dependent PL data for the dilute magnetic semiconductor (DMS) sample T580 (Mn content = 1%) is shown. The excitation used was a 20 mW Argon-ion laser. Temperature of the sample was 1.5 K. We used a room temperature silicon detector. The spectrometer grating used had a groove density of 300 g/mm and a blaze wavelength of 1 μm . The input and output slits of the spec-

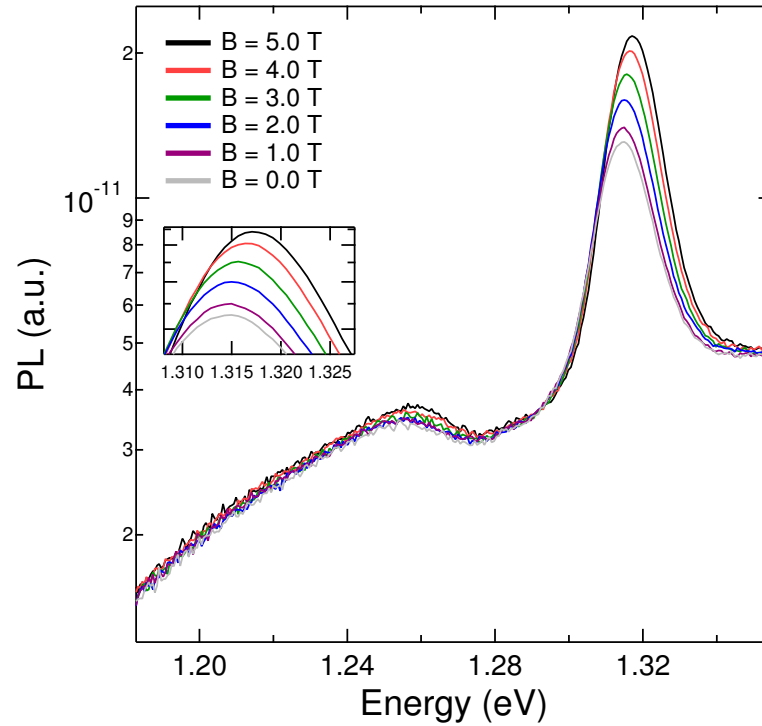


Figure 5.3 : Magnetic field dependant PL data for the dilute magnetic semiconductor (DMS) sample

trometer were set to $500 \mu\text{m}$. The lock-in time constant was 100 ms, with the dwell time at each frequency (controlled by the computer) set to 400 ms. The PL signal is due to the InGaAs layer and not due to the magnetic layer. The shift observed is a diamagnetic shift caused by increasing the confinement of the excitons by the magnetic field.

5.2 Temperature Dependent PL

Figure 5.4 shows the temperature dependent PL data for sample 209B. The excitation used was a 20 mW Argon-ion laser. Temperature of the sample was 1.5 K. We used

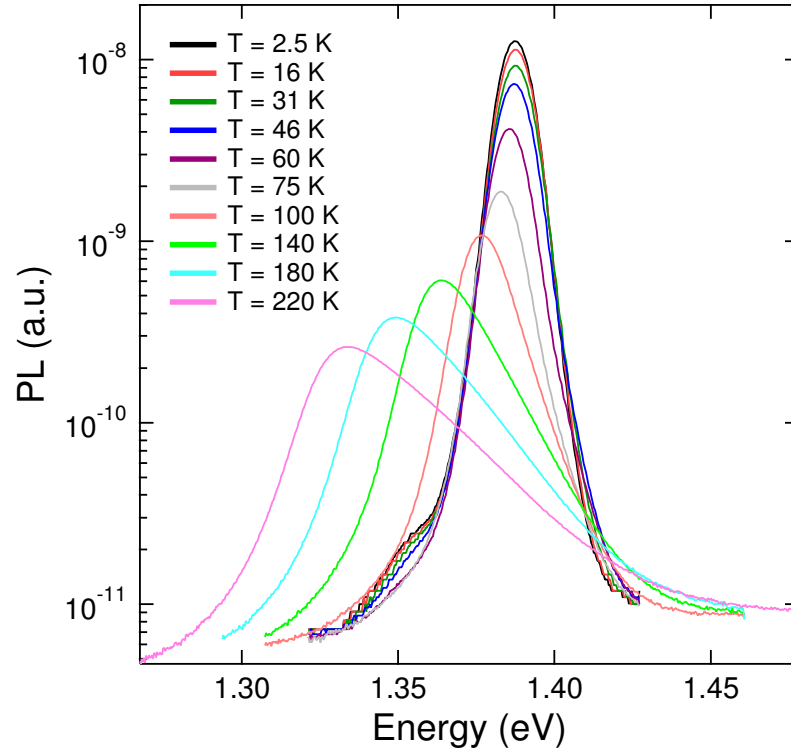


Figure 5.4 : Temperature dependant PL data for InGaAs/AlGaAs MQW sample

a room temperature silicon detector. The spectrometer grating used had a groove density of 1200 g/mm and a blaze wavelength of 750 nm. The input and output slits of the spectrometer were set to 500 μm . The lock-in time constant was 100 ms, with the dwell time at each frequency (controlled by the computer) set to 400 ms.

The red shift in the peak position is observed due to the shrinking of the band edge with increase in temperature. The increased exciton-phonon interaction causes the increase in the line width of emission.

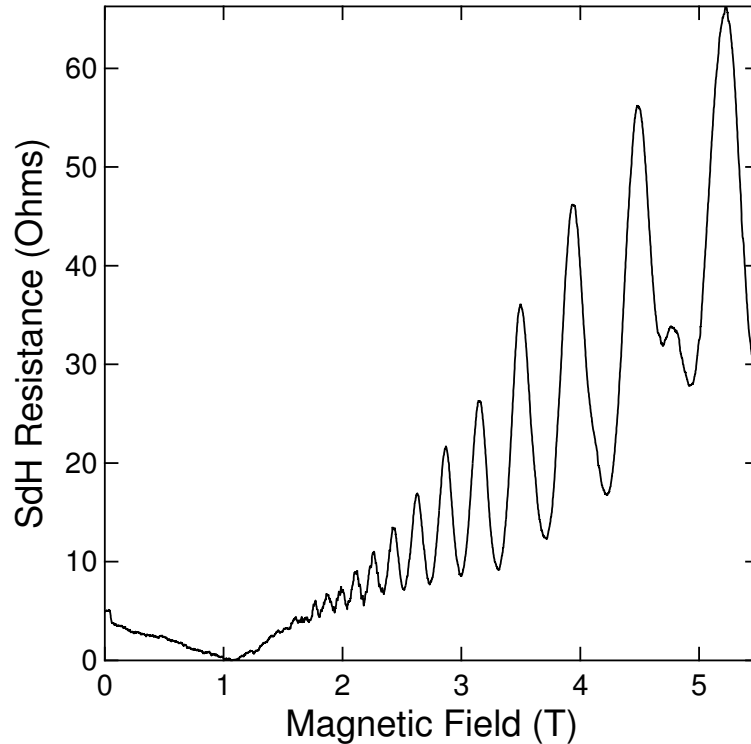


Figure 5.5 : Shubnikov-de Haas effect in InGaAs/AlGaAs MQW sample

5.3 Shubnikov-de Haas (Magneto-Transport) Effect

The Shubnikov-de Haas (SdH) effect is a magnetotransport phenomenon that occurs in intense magnetic fields. The signature of the effect is a periodic waveform when plotted as a function of the inverse magnetic field. The “frequency” of the magnetoresistance oscillations indicates the area of an extremal Fermi surface. Figure 5.5 shows Shubnikov-de Haas effect in the sample 209B. Temperature of the sample was 1.5 K.

Our sample measurements show that the frequency of magnetoresistance oscillations is $3.24 \times 10^{-2} \text{ T}^{-1}$. The area of extremal Fermi surface is found to be $1.39 \times$

10^{12} cm^{-2} .

5.4 Optically Detected Resonance

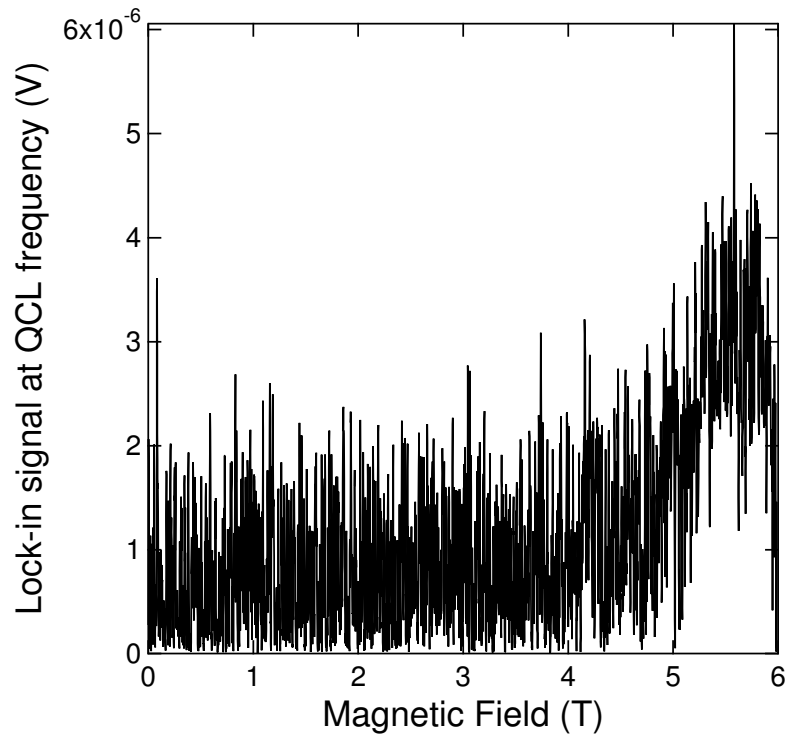


Figure 5.6 : Preliminary ODR data for InGaAs/AlGaAs MQW sample

Figure 5.6 shows the ODR data we took for sample 209B. The excitation used was a 20 mW Argon-ion laser. The QCL current was set to 650 mA, chopped at 75 Hz and duty cycle of 40%. Temperature of the sample was 20 K. We used a room temperature silicon detector. The spectrometer grating used had a groove density of 300 g/mm and a blaze wavelength of $1 \mu\text{m}$. The input and output slits of the spectrometer were set to 1.5 mm. The lock-in time constant was 100 ms, with the

dwell time at each frequency (controlled by the computer) set to 400 ms. The signal was recorded for forward and reverse sweeps of the magnet.

We can see a clear change in PL signal measured at the modulation frequency of the QCL. The data that we measured is noisy. We tried to increase the signal-to-noise ratio but the QCL stopped working shortly after that. The possible reasons for this failure could be the device getting damaged due to repeated thermal cycling and heating due to operation for long periods of time in the CW mode. The resonance observed is most likely to be $1s \rightarrow 2p_+$ transition of the excitons. However, we are still not certain about the resonance mechanism and more work needs to be done to validate our initial observations.

Chapter 6

Summary and Future Work

We have demonstrated that it is possible to observe ODR in semiconductor nanostructures with our present setup. We could not take data more extensively as our THz QCL stopped working during the course of our experiments. However, there are many possibilities that can be explored with the present setup.

6.1 ODTR Study of Other Nanostructures

In the present work we have studied the InGaAs/AlGaAs MQWs. However, there are other samples, discussed previously, that have shown a strong PL and hence are good candidates for ODTR spectroscopy. These samples include AlGaAs/GaAs MQWs and GaAs high mobility 2-DEG samples.

6.2 Spin Resonance Studies

The first ODR studies of semiconductors were done by measuring changes in polarization [6]. Our setup can be adapted with minimal effort for these measurements by creating spin-polarized carriers using circularly polarized light. And instead of measuring the change in magnitude of the PL peak, polarization changes of the emission signal can be measured using a balanced detector arrangement. This would further extend the capability of our system to measure ODESr.

A method to measure the decoherence time T_2 of a single electron spin in a semiconductor quantum dot based on optically detected resonance has been proposed

recently [36]. The spin decoherence time T_2 is related to the loss of phase coherence of a single spin that is prepared in a superposition of its eigenstates. Experimental T_2 measurements of single spin in quantum dots are desirable for quantum information processing applications as it is the limiting time scale for coherent spin manipulation. For such an experiment, circularly polarized laser excitation would be used. Pauli blocking would cause the optical excitation of only one of the electron-spin states. It has been shown that the linewidth of the photoluminescence as a function of the resonance field frequency provides a lower bound on T_2 [36]. It has also been suggested that with the use of a pulsed laser and CW resonance excitation, electron-spin Rabi oscillations can be detected via photoluminescence [36].

6.3 ODTR Study of Excitons in Carbon Nanotubes

We propose to use our QCL-ODR system to further reveal the fundamental properties of 1-D excitons in single-walled carbon nanotubes (SWNTs). 1-D excitons are expected to behave very differently from excitons in higher dimensions: the binding energy of excitons in an ideal 1-D system is infinite [37] and the Sommerfeld factor is less than unity [38].

1-D excitons in SWNTs seem to be even more peculiar. All recent experimental data for interband transitions (absorption and PL) in SWNTs indicate that excitation energies are higher than those expected from band structure calculations. This blue shift contradicts the conventional wisdom that excitonic binding should red shift the excitation energy from the band edge.

Recent theoretical studies [39] indicate that there is a significant blue shift from the single-particle band gap (from tight-binding calculations) due to quasi-particle corrections. This blue shift is expected to exceed the excitonic binding energy, and thus the net effect is a blue shift.

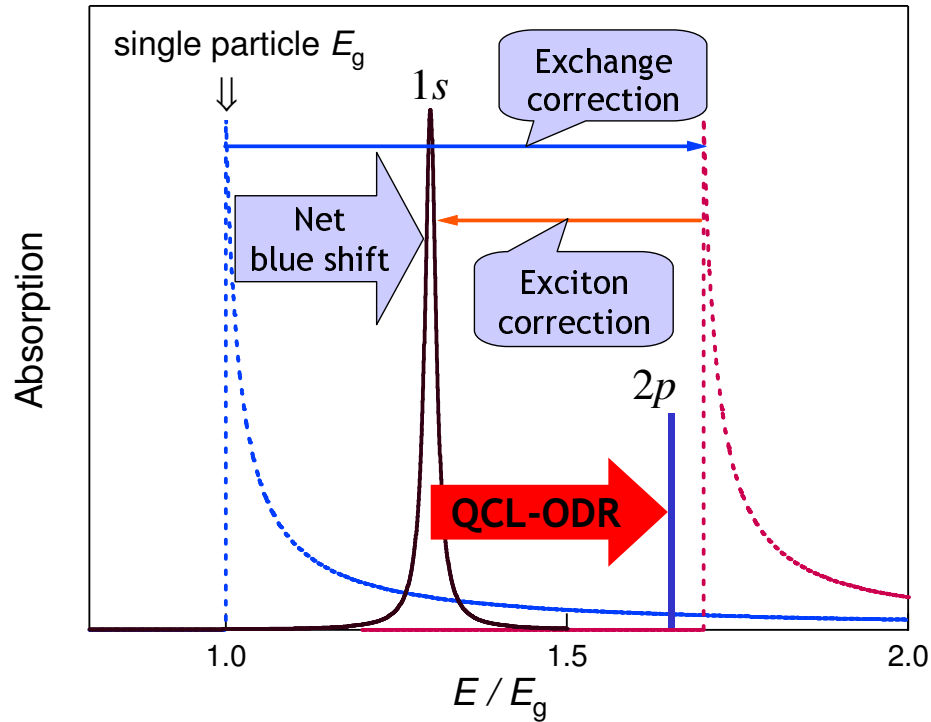


Figure 6.1 : A schematic diagram showing how the interband excitation energies are higher than the calculated bandgaps

Although this model qualitatively works for explaining the unexpectedly blue-shifted interband excitation energies, the magnitudes of these corrections and their dependence on tube diameters, magnetic field, dielectric constant of the surrounding, etc. have not been measured or understood.

We will perform ODR on micelle-suspended SWNTs to observe the $1s \rightarrow 2p_+$ exciton internal transition. As the applied field B increases, the $1s$ state decreases in energy due to the Aharonov-Bohm (AB) effect [40]. While the $2p$ state also decreases, its rate of change with B is smaller [39], and thus, the $1s$ - $2p$ energy separation is expected to increase with increasing B . Therefore, if the QCL energy is slightly higher than the zero-field $1s$ - $2p$ energy, it is expected to show a resonance. This is similar to

what has been observed in donors and excitons in semiconductor structures, although the use of the AB effect here is totally different from the previous studies. The determination of the 1s-2p energy directly provides an estimate of the exciton binding energy.

Bibliography

- [1] R. Köhler, A. Tredicucci, F. Beltram, H. E. Beere, E. H. Linfield, A. G. Davies, D. A. Ritchie, R. C. Iotti, and F. Rossi, “Terahertz semiconductor-heterostructure laser,” *Nature* **417**, 156 (2002).
- [2] D. Mittleman, *Sensing with Terahertz Radiation* (Springer, 2002).
- [3] B. C. Cavenett, “Optically detected magnetic resonance (O.D.M.R.) investigations of recombination processes in semiconductors,” *Advances in Physics* **30**, 475 (1981).
- [4] G. Lampel, “Nuclear Dynamic Polarization by Optical Electronic Saturation and Optical Pumping in Semiconductors,” *Phys. Rev. Lett.* **20**, 491 (1968).
- [5] R. R. Parsons, “Band-to-Band Optical Pumping in Solids and Polarized Photoluminescence,” *Phys. Rev. Lett.* **23**, 1152 (1969).
- [6] C. Hermann and G. Lampel, “Measurement of the g Factor of Conduction Electrons by Optical Detection of Spin Resonance in p -Type Semiconductors,” *Phys. Rev. Lett.* **27**, 373 (1971).
- [7] P. G. Baranov, Y. P. Veshchunov, R. A. Zhitnikov, N. G. Romanov, and Y. G. Shreter, “Optical Detection of Microwave Resonance in Germanium by Means of Luminescence of Electron-Hole Drops,” *JETP Lett.* **26**, 249 (1977).
- [8] R. Romestain and C. Weisbuch, “Optical Detection of Cyclotron Resonance in Semiconductors,” *Phys. Rev. Lett.* **45**, 2067 (1980).

- [9] I. J. Booth and C. F. Schwerdtfeger, "Optically Detected Resonance in AgBr," *Phys. Stat. Sol.* **130**, 749 (1985).
- [10] I. J. Booth and C. F. Schwerdtfeger, "Optical Detection of Cyclotron Resonance in GaP and ZnTe," *Solid State Comm.* **55**, 817 (1985).
- [11] B. C. Cavenett and E. J. Pakulis, "Optically Detected Cyclotron Resonance in GaAs/Ga_{0.67}Al_{0.33}As Superlattice," *Phys. Rev. B* **32**, 8449 (1985).
- [12] E. J. Pakulis and G. A. Northrop, "Optically Detected Electron Cyclotron Resonance in Silicon," *Appl. Phys. Lett.* **50**, 1672 (1987).
- [13] T. Ohyama, T. Tomaru, and E. Otsuka, "Optically Detected Cyclotron Resonance in Ge, Si and ZnSe," *Physica B* **184**, 141 (1993).
- [14] T. Tomaru, T. Ohyama, and E. Otsuka, "Optically Detected Cyclotron Resonance of Exciton and Electron-Hole Droplet Systems in Pure Germanium," *J. Phys. Soc. Jpn.* **58**, 3718 (1989).
- [15] M. G. Wright, N. Ahmed, A. Koohian, K. Mitchell, G. R. Johnson, B. C. Cavenett, C. R. Pidgeon, C. R. Stanley, and A. H. Kean, "Far-Infrared Optically Detected Cyclotron Resonance Observation of Quantum Effects in GaAs," *Semicond. Sci. Tech.* **5**, 438 (1990).
- [16] A. Moll, C. Wetzel, B. K. Meyer, P. Omling, and F. Scholz, "Microwave and Far-Infrared Induced Optically Detected Cyclotron Resonance in Epitaxial InP and GaAs," *Phys. Rev. B* **45**, 1504 (1992).
- [17] J. G. Michels, R. J. Warburton, R. J. Nicholas, J. J. Harris, and C. T. Foxon, "Optically Detected Cyclotron Resonance of GaAs Quantum Wells: Effective-mass Measurements and Offset Effects," *Physica B* **184**, 159 (1992).

- [18] P. Omling, C. Wetzel, A. L. Efros, and B. K. Meyer, “Magneto-Optical and Far-Infrared Optically Detected Cyclotron Resonance Determination of Effective Mass in $\text{GaAs}_{1-x}\text{P}_x$,” *Physica B* **184**, 164 (1993).
- [19] J. G. Michels, R. J. Warburton, R. J. Nicholas, and C. R. Stanley, “An optically detected cyclotron resonance study of bulk GaAs,” *Semicond. Sci. Tech.* **9**, 198 (1994).
- [20] J. Kono, S. T. Lee, M. S. Salib, G. S. Herold, A. Petrou, and B. D. McCombe, “Optically detected far-infrared resonances in doped GaAs quantum wells,” *Phys. Rev. B* **52**, 8654 (1995).
- [21] J. Černe, J. Kono, M. S. Sherwin, M. Sundaram, A. C. Gossard, and G. E. W. Bauer, “Terahertz Dynamics of Excitons in GaAs/AlGaAs Quantum Wells,” *Phys. Rev. Lett.* **77**, 1131 (1996).
- [22] M. S. Salib, H. A. Nickel, G. S. Herold, A. Petrou, and B. D. McCombe, “Observation of Internal Transitions of Confined Excitons in GaAs/AlGaAs Quantum Wells,” *Phys. Rev. Lett.* **77**, 1135 (1996).
- [23] C. Weisbuch and C. Hermann, “Optical detection of conduction-electron spin resonance in GaAs, $\text{GaIn}_{1-x}\text{In}_x\text{As}$, and $\text{Ga}_{1-x}\text{Al}_x\text{As}$,” *Phys. Rev. B* **15**, 816 (1977).
- [24] R. F. Kazarinov and R. A. Suris, “Theory of electrical and electromagnetic properties of semiconductors with superlattices,” *Fiz. Tekh. Poluprov.* **5**, 797 (1971).
- [25] J. Faist, F. Capasso, D. L. Sivco, C. Sirtori, A. L. Hutchinson, and A. Y. Cho, “Quantum Cascade Laser,” *Science* **264**, 553 (1994).

- [26] C. Gmachl, F. Capasso, D. L. Sivco, and A. Y. Cho, “Recent progress in quantum cascade lasers and applications,” *Rep. Prog. Phys.* **64**, 1533 (2001).
- [27] J. Faist, L. Ajili, G. Scalari, M. Giovannini, M. Beck, M. Rochat, H. Beere, A. G. Davies, E. H. Linfield, and D. Ritchie, “Terahertz quantum cascade lasers,” *Phil. Trans. R. Soc. Lond. A* **362**, 215 (2003).
- [28] M. Rochat, J. Faist, M. Beck, U. Oesterle, and M. Ilegems, “Far-infrared ($\lambda = 88 \mu\text{m}$) electroluminescence in a quantum cascade structure,” *Appl. Phys. Lett.* **73**, 3724 (1998).
- [29] B. S. Williams, H. Callebaut, S. Kumar, Q. Hu, and J. L. Reno, “3.4-THz quantum cascade laser based on longitudinal-optical-phonon scattering for depopulation,” *Appl. Phys. Lett.* **82**, 1015 (2003).
- [30] G. Scalari, L. Ajili, J. Faist, H. Beere, E. Linfield, D. Ritchie, and G. Davies, “Far-infrared ($\lambda \simeq 87 \mu\text{m}$) bound-to-continuum quantum cascade lasers operating up to 90 K,” *Appl. Phys. Lett.* **82**, 3165 (2003).
- [31] J. Faist, D. Hofstetter, M. Beck, T. Aellen, M. Rochat, and S. Blaser, “Bound-to-Continuum and Two-Phonon Resonance Quantum Cascade Lasers for High Duty Cycle, High Temperature Performance,” *J. Quant. Electron.* **38**, 533 (2003).
- [32] D. Smirnov, C. Becker, O. Drachenko, V. V. Rylkov, H. Page, J. Leotin, and C. Sirtori, “Control of electron-optical phonon scattering rates in quantum box cascade lasers,” *Phys. Rev. Lett.* **66**, 121305 (2002).
- [33] V. Tamosiunas, R. Zobl, G. Fasching, J. Ulrich, K. Unterrainer, R. Colombelli, C. Gmachl, K. West, L. Pfeiffer, and F. Capasso, “Terahertz quantum-cascade lasers in a magnetic field,” *Appl. Phys. Lett.* **83**, 3873 (2003).

- [34] G. Scalari, S. Blasér, L. Ajili, J. Faist, H. Beere, E. Linfield, D. Ritchie, and G. Davies, “Population inversion by resonant magnetic confinement in terahertz quantum cascade lasers,” *Appl. Phys. Lett.* **83**, 3453 (2003).
- [35] L. Ajili, G. Scalari, D. Hofstetter, M. Beck, J. Faist, H. Beere, G. Davies, E. Linfield, and D. Ritchie, “Continuous-wave operation of far-infrared quantum cascade lasers,” *Elec. Lett.* **38**, 1675 (2002).
- [36] O. Gywat, H.-A. Engel, D. Loss, R. J. Epstein, F. M. Mendoza, and D. D. Awschalom, “Optical detection of single-electron spin decoherence in a quantum dot,” *Phys. Rev. B* **69**, 205303 (2004).
- [37] R. Loudon, “One-Dimensional Hydrogen Atom,” *Am. J. Phys.* **27**, 649 (1959).
- [38] T. Ogawa and T. Takagahara, “Interband Absorption Spectra and Sommerfeld Factors of a One-Dimensional Electron-Hole System,” *Phys. Rev. B* **43**, 14325 (1991).
- [39] T. Ando, “Excitons in Carbon Nanotubes,” *J. Phys. Soc. Jpn.* **66**, 1066 (1997).
- [40] S. Zaric, G. N. Ostojic, J. Kono, J. Shaver, V. C. Moore, R. H. Hauge, R. E. Smalley, and X. Wei, “Optical signatures of the Aharonov-Bohm Phase in Single-Walled Carbon Nanotubes,” *Science* **304**, 1129 (2004).